Ore Geology Reviews 164 (2024) 105858

Contents lists available at ScienceDirect

Ore Geology Reviews

journal homepage: www.elsevier.com/locate/oregeorev

Geochronology, geochemistry, and tectonic setting of the Neoproterozoic magmatic rocks in Pan-African basement, West Ethiopia

Junaid KHAN [a,b,c], Hua-Zhou Yao [a,b,*], Jun-Hong Zhao [c], Asma TAHIR [b], Kai-Xu Chen [a], Jian-Xiong Wang [a], Fang Song [a], Jing-Yin Xu [e], Ismail Shah [d]

[a] China Geological Survey, Wuhan Center, 430205 Hubei, China
[b] Institute of Geological Survey, China University of Geosciences, Wuhan 430074, China
[c] State Key Laboratory of Geological Processes and Mineral Resources, China University of Geosciences, Wuhan 430074, China
[d] School of Earth Science, China University of Geosciences, Wuhan 430074, China
[e] Geophysical Exploration Brigade of Hubei Geological Bureau, Wuhan 430056, Hubei, China

ARTICLE INFO

Keywords:
Pan-African basement
Intrusive and meta-intrusive rocks
Neoproterozoic tectonic stages
Juvenile crust
Depleted mantle source

ABSTRACT

The West Ethiopian plateau lies in the transition zone between the Arabian-Nubian shield and the Mozambique belt of the Pan-African orogen, underlain by Precambrian to Tertiary rocks in the Gimbi-Nejo area. The Precambrian basement consists mainly of intrusive-meta-intrusive and meta-sedimentary rocks with ice-rafting deposits. Based on the field survey, unique material records, deformation features, magmatism, and metamorphism indicate that the Gimbi-Nejo area likely underwent four tectonic stages during the Neoproterozoic era.

The sedimentary formation of 980 ± 3.9 Ma rift valleys is represented by meta-clastic rocks, calc-silicate rocks, meta-basic rocks bearing marble in Chochi, and the Kata domain. Geochemically, meta-peridotite and meta-gabbros show tholeiitic features, while meta-granitoids are medium-K calc-alkaline peraluminous to metaluminous A-type (Ce/Nb 2.1–11.9; Y/Nb 1.2–8; Yb/Ta 2.6–14). Meta-gabbro samples with immobile HFSE (Th, Ta, Hf) and REE (La, Sm, Yb) fall in the within-plate alkaline basalt, oceanic island basalt (OIB), and continental rift basalt field. Meta-granitoid samples also fall in the within-plate granite field. The lithospheric subduction stage magmatic arc, composed of gabbros and granitoids, was emplaced around 827 ± 3.2 Ma. The granitoids include calcic tonalite and trondhjemite showing an adakitic signature with high Sr/Y (14.2–48.2) ratios. Gabbro samples fall in the island arc basalt and continental arc basalt field. Meta-peridotites and meta-gabbros to gabbros originated from the partial melting of garnet-spinel lherzolite to spinel lherzolite (<10 %) and garnet lherzolite to garnet-spinel lherzolite (<30 %) mantle source, respectively. The continental collisional area contains thrust folds and faults trending in a north–south direction. The ca. 797 ± 3.7 Ma calc-alkalic granitoid rocks along the suture zone are high-K peraluminous I-type granitoids (ASI < 1.1). The strike-slippage area is represented by sinistral ductile shearing deformation. The alkali-calcic granitoid rocks associated with shearing and decollements are low to high-K calc-alkaline peraluminous-metaluminous I-S type granitoids (ASI = 0.95–1.17). The U-Pb age of alkali-calcic granitoid is 564 ± 3.4 Ma. Syn-collisional calc-alkalic and late-post orogenic alkali-calcic granitoid samples both fall within the category of within the plate granite.

The εHf (t) values of meta-granitoid (+9.4 to + 15.5), calcic granitoid (+7.6 to + 13.2), calc-alkalic granitoid (+7.4 to + 15.5), and alkali-calcic granitoid (+7.11 to + 17.12) suggest that these Neoproterozoic granitoids have been derived from a Meso-Neoproterozoic juvenile crust that formed through depleted mantle source. Depleted mantle magma likely ascended to the juvenile crust and remained there for a certain period (mean time = 122 Ma, 257 Ma, 248 Ma, and 256 Ma, respectively).

1. Introduction

The Neoproterozoic era was a time of significant tectonic activity, marked by the formation of several supercontinents, widespread orogenic events, and glaciation (Hoffman et al., 2017).

The plate tectonic system of the Neoproterozoic era has been

* Corresponding author at: China Geological Survey, Wuhan Center, 430205 Hubei, China.
E-mail addresses: ycxc2009@126.com, Junaidkhan5615@yahoo.com (H.-Z. Yao).

https://doi.org/10.1016/j.oregeorev.2023.105858
Received 15 April 2023; Received in revised form 22 December 2023; Accepted 23 December 2023
Available online 29 December 2023

explored by various authors (e.g., Kazmin, 1971; 1975; Kazmin et al., 1978; Vail, 1985; Tadesse, 1996; Tadesse-Alemu, 1998) to enhance understanding. However, persistent irregularities, intermittent findings, and lingering unanswered questions, such as those related to geochemical data within the context of prevailing geological models, still pose challenges in fully unraveling the petrological evolution of Neoproterozoic magmatic systems.

One of the key events in Neoproterozoic era was the formation and breakup of the supercontinent Rodinia. It began in late Mesoproterozoic and continued into early Neoproterozoic, approximately 1.26–0.90 billion years ago (Kee et al., 2019). The evidence for the breakup of Rodinia is evident in numerous regions worldwide, encompassing the North American mid-continent rift system, the Grenville orogen in eastern North America, the rift basins of East Africa, the sedimentary basins of South America, among others (Condie, 2005; Tollo et al., 2004). In addition to extensional tectonics, compressional tectonic settings also developed during the Neoproterozoic era, particularly during the assembly of the Gondwana. This process involved the collision of several continental blocks, leading to the formation of orogenic belts, such as the Pan-African orogeny (Stern, 1994), the Kuunga orogeny (Axelsson et al., 2020) and the Malagasy orogeny (Collins et al., 2018) in Africa, the Brasiliano orogeny in South America (Cawood and Buchan, 2007), and Ruker and Lutzow-Holm Complexes in Antarctica (Ferraccioli et al., 2011). On the earth after Grenville orogeny, Pan-African orogen (PAO) is the largest orogenic belt (Rino et al., 2008). The recorded time period of Cadomian and Baikalian orogen in Europe and Asia, respectively is similar to PAO (Kröner, 2004). Overall, the tectonic setting of the Neoproterozoic era was complex and multifaceted, and its study has provided important insights into the evolution of the Earth's crust and the development of the continents.

Magmatic and metamorphic events were also widespread during the Neoproterozoic era. Magmatic rocks provide crucial insights into the dynamic processes that governed Earth's lithospheric evolution. The Pan-African orogen in Africa specially in West Ethiopia was associated with the emplacement of several large plutonic bodies, and the development of high-grade metamorphic rocks (Kazmin, 1971; Abraham, 1989; Abdelsalam and Stern, 1996; Asrat et al., 2001; Allen and Tadesse, 2003; Tadesse and Allen, 2005; Frost et al., 2001).

Pan-African orogenic magmatic (intrusive-meta intrusive) basement rocks are exposed in the Gimbi-Nejo area, western Ethiopia and are in better conditions for the geochemical studies. Several researchers (e.g., Kazmin, 1971; 1973; 1975; Kazmin et al., 1978; Vail, 1985; Tadesse, 1996; Tadesse-Alemu, 1998, etc.) have examined the basement rocks in west Ethiopia. However, more comprehensive investigations are required, including in-depth studies on magma sources, compositions, and tectonic boundaries. These studies should incorporate previously unmapped rock bodies data that were left unexplored due to the impact of warfare. In this investigation, previously unmapped intrusive-meta intrusive rock samples from various locality within the Gimbi-Nejo region, located in western Ethiopia, were systematically collected during field mapping. The primary objective of this study was to assess the petrogenesis and unravel the tectonic framework across temporal scales, utilizing analyses of elemental and isotopic data.

2. Geological setting

2.1. Regional geology

The Pan-African orogenic belt is comprised of mainly high-grade metamorphic gneiss (MB: Mozambique belt) in the south and low-grade metamorphosed volcanics and sedimentary rocks (ANS: Arabian-Nubian shield) in the north (Stern, 1994; Yibas et al., 2002; Woldemichael et al., 2010; Abbate et al., 2015). West Ethiopia lies at the junction of ANS and MB. Pre-, syn-, and post-tectonic activity is responsible for the intrusion of magmatic rocks inside the West Ethiopian basement (Kazmin, 1973; Tadesse, 1996; Asrat et al., 2001). Pre-tectonic setting in western Ethiopia involved meta-volcanic, meta-sedimentary, and migmatitic gneissic terrane while syn- to post-tectonic setting involved gabbroic to granitic intrusions (Johnson et al., 2004; Woldemichael et al., 2010).

The West Ethiopian geology is complex and dominated by a sequence of Precambrian to Phanerozoic rocks, which have been deformed and metamorphosed by tectonic activity (Alemu and Abebe, 2000). The oldest rocks in the region are Archean to Proterozoic basement rocks. These rocks include gneisses, granites, and schists, and are intruded by several granitic and syenitic plutons (Alemu and Abebe, 2000; Junaid et al., 2022). Overlying the basement rocks are a sequence of sedimentary and volcanic rocks, which were deposited during the Neoproterozoic era to Paleozoic periods. These rocks include sandstones, shales, limestones, and volcanic tuffs, and are folded and faulted (Alemu and Abebe, 2000).

In the Cenozoic era, the region was affected by rifting and volcanism associated with the breakup of continent. This resulted in the deposition of a thick sequence of volcanic and sedimentary rocks, including the Oligocene to Miocene volcano-sedimentary sequence which fills the Western rift (Hardarson, 2015; Khan et al., 2023). This rift is characterized by active faulting and volcanism, which has created a complex landscape of rift valleys, volcanoes, and highlands (Hardarson, 2015). Overall, the regional geology of West Ethiopia is characterized by active rifting and faulting, which has created a diverse geological landscape with a long and complex history.

2.2. Local geology

The Gimbi-Nejo area in west Ethiopia is mainly composed of Pan-African orogenic basement rocks, which include Precambrian metamorphic rocks and intrusive igneous rocks overlaid by Paleozoic sedimentary rocks, Tertiary volcanic rocks, and Quaternary deposits (Fig. 1). Geochemical prospecting data indicates the presence of elevated economic potential minerals concealed within the basement rocks of West Ethiopia (Junaid et al., 2022). In the area, different types of intruded rocks with different deformation features indicate distinct tectonic stages. The Precambrian intrusive-meta intrusive and meta-sedimentary rock units exposed cover almost 85 % of the Gimbi-Nejo area (Kazmin, 1971; 1975; Kazmin et al., 1978; Alemu and Abebe, 2000; Asrat et al., 2001; Williams, 2016; Junaid et al., 2022). All these rocks show different deformation patterns and degrees of metamorphism, which vary from high amphibolite facies (Fig. 2g) to low greenschist facies (Fig. 2i) along geological structures. The widely distributed Precambrian metamorphic rocks include migmatitic biotite gneiss, biotite-hornblende gneiss, granitoid orthogneiss, felsic schist, greenschist, meta gabbro-amphibolite, porodite, pelitic, and arenopelitic schist, talc-schist, serpentinized, serpentinized dunite, plagioclase amphibolite, pyroxenite, Abshala mélange slices, marble slices, gabbro-amphibolite slices, quartzite (chert) slices, and meta-mudstone slices (Junaid et al., 2022). All these Precambrian rocks are previously divided into different rock assemblages and domains, like Aba Sina, Chochi, and Kata domains (Alemu and Abebe, 2000). The details of these rock assemblages with lithology, localities, and geological structures are well explained on the modified geological map of the area (Fig. 1b). The field survey in the Kata domain indicates that lamellar or stretching lens meta-conglomerate or graphite sericite schist with breccia occur as interlayers in the graphite sericite unit of the meta-sedimentary rock formation, identified as Neoproterozoic ice rafting deposits (Fig. 2b). The ice rafting deposit, i.e., glaciated breccia, was first discovered in the western Ethiopian plateau. In northern Ethiopia, Saudi Arabia, and Egypt, this kind of breccia, which is regarded as the result of "Snowball Earth," was also found in the Tambien group, Mahd group, and Wadi Kareim area, respectively (Johnson et al., 2002; Beyth et al., 2003; Stern et al., 2006).

Based on previous opinions during the field survey, it is observed that the Gimbi-Nejo area had experienced a regional ductile shear zone

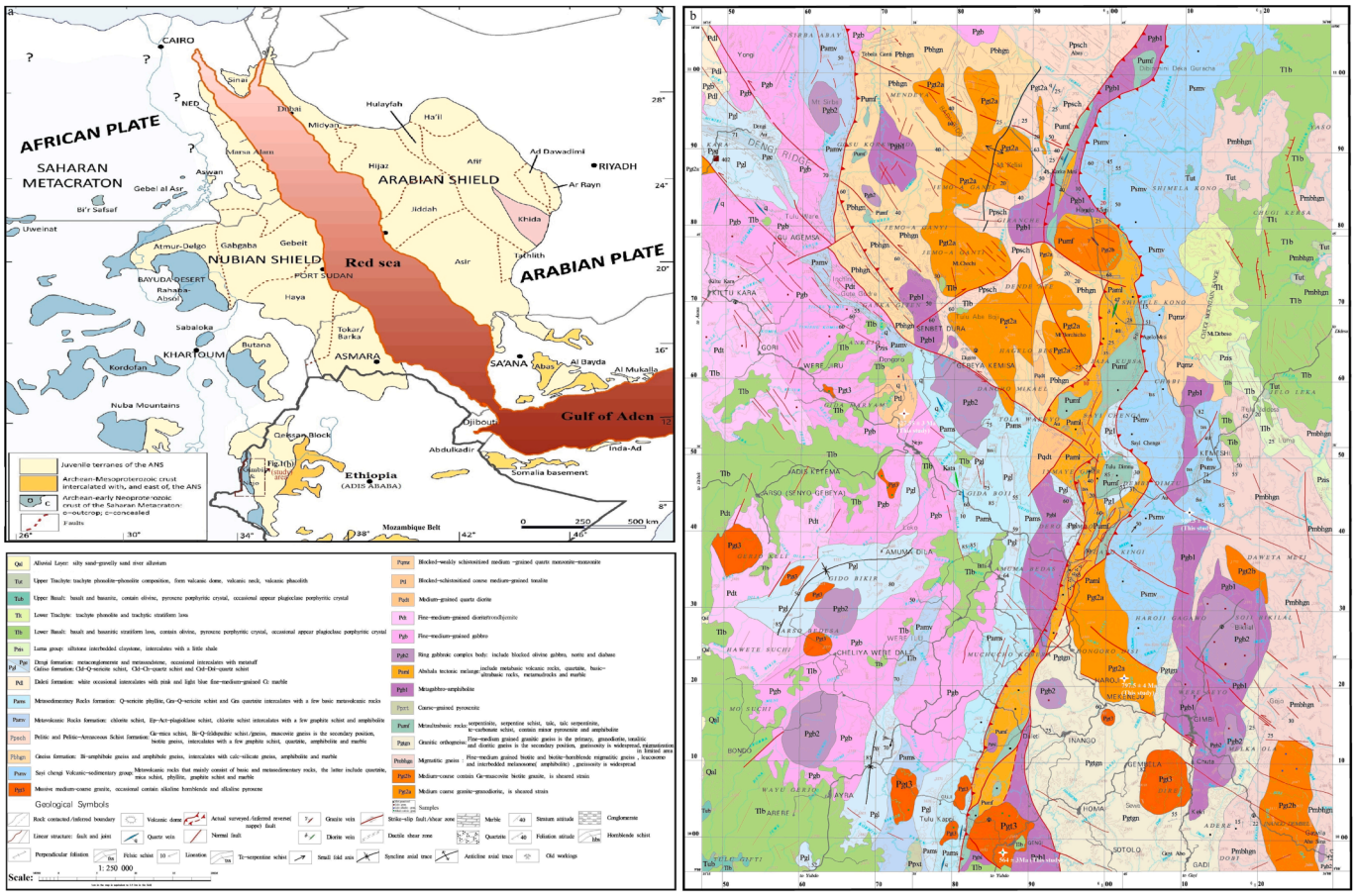

Fig. 1. (a) Ethiopian geomorphological map showing the location of the study area (Gimbi-Nejo) in west Ethiopia (modified after Stern et al., 2006; Woldemichael et al., 2010; Johnson et al., 2011; Fitwi et al., 2019), (b) Showing the geological map of study area.

along north to south trending reverse faults and northwest left-lateral strike-slip faults (Fig. 1b). Along these geological structures, Precambrian intrusive rocks, including gabbro, olivine gabbro, diorite, tonalite (Fig. 2j), quartz monzodiorite, quartz diorite, granite, granodiorite, two-mica granite (Fig. 2h), pyroxenite-bearing gabbro, and hornblendite inclusion in diorite, were also widely distributed.

3. Materials and methods

3.1. Sample collection and Petrographic analysis

The sample collection area is Gimbi-Nejo (9100 km^2) on the western Ethiopian plateau. During the field survey of the study area, we collected sixty-two previously unmapped representative intrusive and meta-intrusive rock samples from four different localities based on the region's deformation pattern, metamorphism, and volcanism. Each sample weighed almost 1000 g and was packed in a sample bag labeled with a unique sample number before being sent to the laboratory for analyses. The sampling localities are indicated on the geological map (Fig. 1b; Table 1 & 2 of supplementary material). The rock sampling sites were selected based on the lithological variation.

Petrographic analysis was performed on specific samples using an optical microscope equipped with a high-resolution Nikon DS Fi3 microscope camera. Relevant photomicrographs were taken using NIS-Elements software (version 4.3). The thin sections of the samples were prepared using standard methods at the China Geological Survey (CGS), Wuhan Center laboratory. Epoxy resin was utilized to affix the segmented samples onto glass slides. Following mounting, the thin sections were meticulously polished to a thickness of 30 μm.

3.2. Zircon U-Pb ages and Hf isotope analysis

Granitoid zircons possess significant value in examining petrogenetic records due to their U-Pb and Lu-Hf isotopic information. This research extracted inclusion-free zircon grains from four granitoid samples, including meta-granitoid (S-449–03), calcic granitoid (S-438-04B), calc-alkalic granitoid (S-478–01), and alkali-calcic granitoid (S-113–01), using conventional magnetic and heavy liquid separation techniques. After the grains were polished, coated, and mounted in epoxy, standard GJ-1 and Plešovice were utilized in the process (Elhlou et al., 2006; Sláma et al., 2008). In the geochemical laboratory of the CGS, Wuhan Center, cathodoluminescence (CL) images of the zircon grains were taken to identify target spots for U-Pb dating analyses, utilizing standard zircon-91500 in ICP-MS. The work procedure for these analyses was explained in detail by Wu et al. (2006) and Liu et al. (2010). Isoplot version 5.2 was then used to generate concordia plots and calculate means with a 1σ error (Ludwig, 2003). Additionally, spots with high concordance were used for Lu-Hf isotopic analyses with the Neptune Plus multi-collector ICP-MS at CGS Wuhan Center. These analyses used a laser beam with a 5.3 J/cm^2 energy density, a 44 μm spot size, and an 8 Hz repetition rate with a 20 s ablation time frame. The ICP-MS employed a mixture of helium and argon gases, and reference materials Plesovice and Penglai were used during the analyses. The detailed work procedure for these analyses has been explained by Hu et al. (2012), and ICP-MS data calibrations (Liu et al., 2010) with a 1σ error were used to handle raw data.

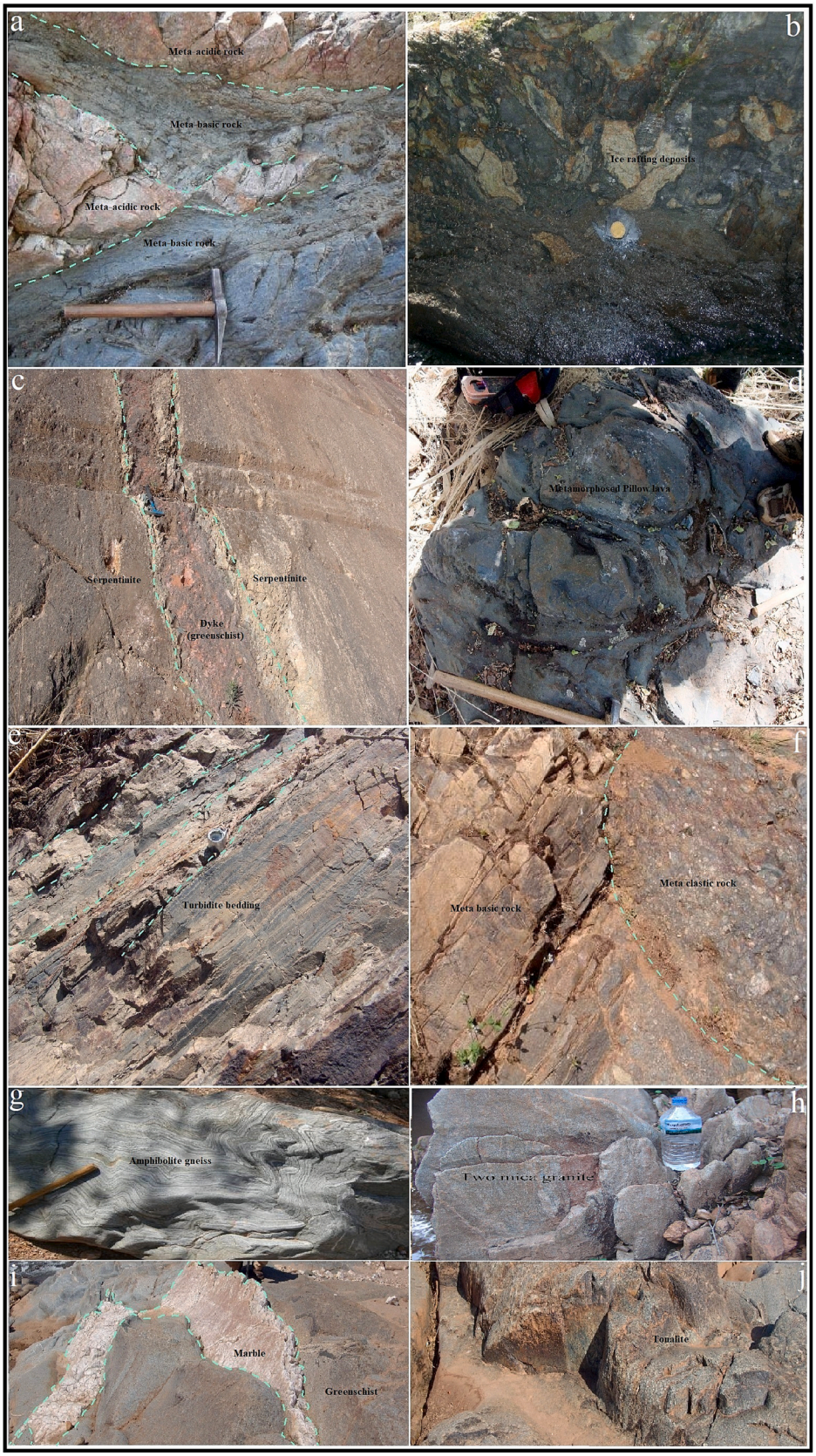

Fig. 2. Photos showing different geological rock features of the study area (a) bimodal *meta*-intrusive rocks in the Sayi chenga group; (b) Ice rafting deposits in metasedimentary rock formation; (c) Dyke stock in In Tulu dimtu tectonic mélange belt; (d) Pillow lava in the Sayi chenga group; (e) Turbidite bedding of *meta*-sandstone slices and *meta*-mudstone slices in Abshala mélange; (f) *meta*-clastic rocks and *meta*-basic rock in Chochi and Kata domain; (g) Amphibolite gneiss in Chochi domain; (h) Tonalitic body in Gia Maryam area; (i) Meta-basic rock bearing marble in Chochi and Kata domain.

3.3. Whole-rock major and trace elements

To conduct analyses on major and trace elements, representative samples underwent drying at 110 °C and were pulverized to a size of 0.074 mm with the use of a planetary ball mill, conducted at the geochemical laboratory of CGS, Wuhan Center. PANalytical Axios Max X-ray fluorescence (XRF) was utilized to analyze major elements in fused glass beads. The Thermo X Series-2 ICP-MS was used to analyze the trace

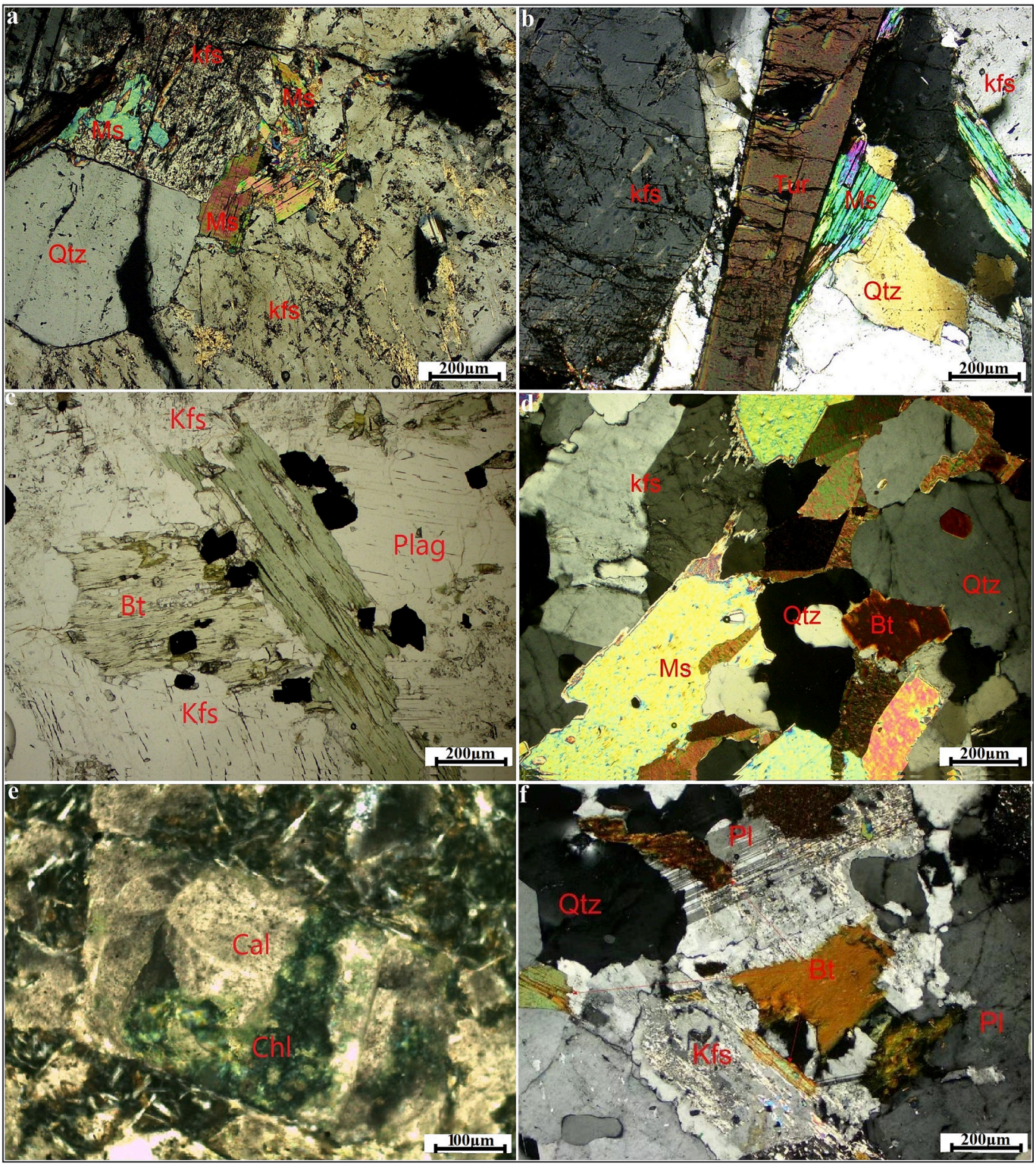

Fig. 3. Photomicrographs of the studied samples. (a) Calc-alkalic granite (S-478–01) with identifiable minerals such as quartz (Qtz), muscovite (Ms), and potassium feldspar (Kfs); (b) Calc-alkalic Granite (S-151–01) featuring quartz (Qtz), muscovite (Ms), potassium feldspar (Kfs), and a secondary mineral, tourmaline (Tur); (c) Alkali-calcic Granite (S-113–01) showcasing potassium feldspar (Kfs), plagioclase (Pl), and biotite (Bt); (d) Alkali-calcic Granite (S-403–02) illustrating quartz (Qtz), muscovite (Ms), biotite (Bt), and potassium feldspar (Kfs); (e) Metamorphosed basic rock (S-447–01) reveals predominant minerals: chlorite (Chl) and calcite (Cal); (f) Calcic Granite (S-437–06) featuring quartz (Qtz), biotite (Bt), potassium feldspar (Kfs), and plagioclase (Pl).

and REE elements. For trace elements, 25 mg of each sample powder underwent digestion in a mixture of HNO_3 and HF, while for rare earth elements (REE), 100 mg of each sample powder underwent digestion in a mixture of HF, HCl, HNO_3, and H_2SO_4 acids. A detailed explanation of the analysis procedures is provided by Coleman (1980) and West (2003). The XRF and ICP-MS analyses displayed accuracies of 1–2 % and 5 %, respectively.

4. Results

4.1. Petrography

The microscopic analysis of rock thin sections provides a unique window into the intricate mineralogical and textural features that shape the Earth's crust. The selected samples of calcic granitoid, calc-alkalic granitoid, and alkali-calcic granitoid exhibit a phaneritic texture, while meta-basic rock shows a porphyritic texture. Mineralogically, calcic, calc-alkalic, and alkali-calcic granites are composed of quartz (40–47 %), muscovite (5–10 %), biotite (0.5–2 %), potassium feldspar (7–30 %), plagioclase (30–42 %), and a secondary mineral—tourmaline (30–40 %; Fig. 3). All these mineral grains are angular to subangular. Plagioclase indicates crystal twinning. Metamorphosed basic rock reveals predominant minerals: chlorite (40–50 %) and calcite (<5 %; Fig. 3). Calcite formation may arise as a result of the alteration of plagioclase, serving as an indicative marker for a high degree of metamorphic grade.

4.2. U-Pb zircon geochronology

The resulting chronological framework contributes to a refined understanding of the temporal distribution and correlation of magmatic events across study area. The U-Pb dating results of zircon grains from meta-granitoid (S-449–03), calcic granitoid (S-438-04B), calc-alkalic granitoid (S-478–01), and alkali-calcic granitoid (S-113–01) are presented in Tables 3–6 of supplementary material and are plotted in Fig. 5. All grains are between 100 and 200 μm in size (Fig. 4). Diverse morphological features are observed, characterized by varying length-to-width ratios and typological distinctions. The Cathodoluminescence (CL) images reveal zonation patterns that are interpreted as igneous origin (Fig. 4). The contents of Th and U in zircons are also indicators of magmatic and metamorphic origin. The metamorphic-grown zircon crystals have a low Th/U ratio, usually 0.05–0.1 (Williams and Claesson, 1987; Maas et al., 1992; Woldemichael et al., 2010). Here zircons of meta-granitoid have a Th/U ratio of 0.26–0.5, calcic granitoid 0.42–0.85, calc-alkalic granitoid 0.39–0.83, and alkali-calcic granitoid 0.33–0.62, which indicates magmatic origin. Twenty-nine analyses were performed on zircons from sample S-449–03, all of which are concordant or nearly concordant (U-Pb = 980.3 ± 3.9 Ma; MSWD = 0.019, n = 29) and yield a weighted average $^{206}Pb/^{238}U$ age of 980.3 ± 3.9 Ma (MSWD = 2.6, n = 29). Similarly, twenty-six analyses were conducted on zircons from sample S-438-04B, resulting in a concordant U-Pb age of 827.6 ± 3.1 Ma (MSWD = 0.0057, n = 26), with a weighted average $^{206}Pb/^{238}U$ age of 827.6 ± 3.2 Ma (MSWD = 1.0, n = 26). Fifteen zircon grains from sample S-478–01 were analyzed and yielded a concordant or nearly concordant U-Pb age of 797.5 ± 3.65 Ma (MSWD = 0.016, n = 15), with a mean weighted age of 797.5 ± 3.7 Ma (MSWD = 6.7, n = 15). Sixteen zircon grains from sample S-113–01 show a concordant or nearly concordant age of 564.8 ± 3.3 Ma (MSWD = 0.02, n = 16), with a weighted mean $^{206}Pb/^{238}U$ age of 564.8 ± 3.4 (MSWD = 1.9, n = 16).

4.3. Lu-Hf isotopic compositions

The in-situ Hf isotopic compositions of meta-granitoid (S-449–03), calcic granitoid (S-438-04B), calc-alkalic granitoid (S-478–01), and alkali-calcic granitoid (S-113–01) zircon grains with concordances of 90–100 % are shown in Tables 7–10 of supplementary material and are plotted in Fig. 10. The $^{176}Hf/^{177}Hf$ ratios of sample S-449–03 zircon grains range from 0.28248 to 0.28267, sample S-438-04B zircon grains from 0.28250 to 0.28275, sample S-478-01 zircon grains from 0.28256 to 0.28281, and sample S-113–01 zircon grains from 0.28264 to 0.28297. Their εHf (t) values range from + 9.4 to + 15.5, +7.6 to + 13.2, +7.41 to + 15.51, and + 7.11 to + 17.12, respectively. The 2-stage (TDM2) model ages range from 849 to 1233 Ma, 863 to 1220 Ma, 698 to 1181 Ma, and 408 to 1043 Ma, respectively.

4.4. Major and trace elements

The major and trace element compositions of the intrusive and meta-intrusive rocks in the study area are shown in Tables 1 & 2 of supplementary material. A total of 29 meta-intrusive rock samples from the area show regular compositional variation. Sixteen *meta*-peridotite rock samples contain high MgO (31–50.12 wt%), Fe_2O_{3T} (1–15 wt%), and low SiO_2 (39.4–62.7 wt%) content with total alkalis (K_2O + Na_2O) 0.02–0.42 wt%. Seven *meta*-gabbro rocks have low MgO (2.65–9.76 wt %), Fe_2O_{3T} (1.2–9.8 wt%), and high SiO_2 (47.13–62.7 wt%) contents with total alkalis (K_2O + Na_2O) 2.29–6.99 wt%. In comparison, six *meta*-granitoid rocks have low MgO (0.1–2.22 wt%), $Fe_2O_3^T$ (2–14.6 wt%), and high SiO_2 (60.72–82.4 wt%) contents with total alkalis (K_2O + Na_2O) 0.070–7.88 wt% (volatile-free).

In mid-oceanic ridge normalized diagrams, *meta*-intrusive samples typically exhibit enrichment in large-ion lithophile elements (LILE) compared to high-field-strength elements (HFSE). These samples show right-inclined chondrite-normalized REE patterns (Fig. 8) in the presence of light rare earth elements (LREE) enrichment. The *meta*-peridotite rock samples display $(La/Yb)_N$ = 2.76–211 and Eu/Eu* = 0.37–0.79; *meta*-gabbro rock has $(La/Yb)_N$ = 1.7–24 and positive to negative Eu anomalies Eu/Eu* = 0.40–0.46; *meta*-granitoid $(La/Yb)_N$ = 4.23–196 and slightly negative Eu anomalies Eu/Eu* = 0.32–0.47. These medium K calc-alkaline peraluminous to metaluminous *meta*-granitoids are trending toward A-type granitoid zone in the plot (Fig. 7c, d, h).

Thirty-three intrusive rock samples from the area also show regular compositional variation. The pyroxene bearing gabbro (S-464–01) sample contains SiO_2 (48.5 wt%), MgO (21.7 wt%), and K_2O (0.25 wt%) contents with total alkalis (K_2O + Na_2O) 1.0 wt%. Twelve gabbro samples have variable SiO_2 (41.2–51.3 wt%), MgO (4.7–19.6 wt%), and K_2O (0.02–1.17 wt%) contents with total alkalis (K_2O + Na_2O) 0.06–4 wt%. These gabbro rocks show a right-inclined chondrite-normalized REE pattern (Fig. 8) in the presence of LREE enrichment. $(La/Yb)_N$ = 1.4–7.9 and positive Eu anomalies Eu/Eu* = 0.85–3.1 for gabbro rocks. These gabbro rock samples are enriched in LILE than HFSE (Figs. 8 & 10).

The representative granitoid rock samples in the major-element-based classification (SiO_2 vs. Na_2O + K_2O-CaO) are mainly distributed into calc, calc-alkalic, and alkali-calcic zones (Fig. 7e). Six calcic granitoid rock samples have variable SiO_2 (54.5–74.8 wt%), MgO (0.39–3.9 wt%), and K_2O (0.11–1.26 wt%) contents with total alkalis (K_2O + Na_2O) of 4.3–7.4 wt%. Five calc-alkalic granitoid samples display high and restricted SiO_2 (70.5–75.5 wt%), Al_2O_3 (12.7–15.14 wt%), and K_2O + Na_2O (7.2 – 8.74 wt%). In contrast, nine alkali-calcic granitoid samples display a wide range of SiO_2 (60.3–77.32 wt%) and K_2O + Na_2O (2–9.6 wt%) but a relatively short range of Al_2O_3 (11.01–15.6 wt%). The majority of calc-alkalic and alkali-calcic granitoid samples show high-K calc-alkaline affinities, while calc-granitoids show low-medium K tholeiite affinities (Fig. 7d). Both calcic and calc-alkalic granitoids have higher alumina saturation than the alkali-calcic granitoid, indicating I-type peraluminous and I-S type peraluminous-metaluminous, respectively (Fig. 7c, f). The samples of calcic, calc-alkalic, and alkali-calcic granitoid show right-inclined chondrite-normalized REE patterns in the presence of light rare earth elements (LREE) enrichment ($[La/Yb]_N$ = 3.6–7.1, 0.4–37.3 & 0.4–12; Eu/Eu* = 0.89–1.65, 0.1–1.7 & 0.4–13.3, respectively; Fig. 8). On the primitive mantle-normalized plot, the calcic granitoids are enriched in LILE than HFSE, calc-alkalic granitoid

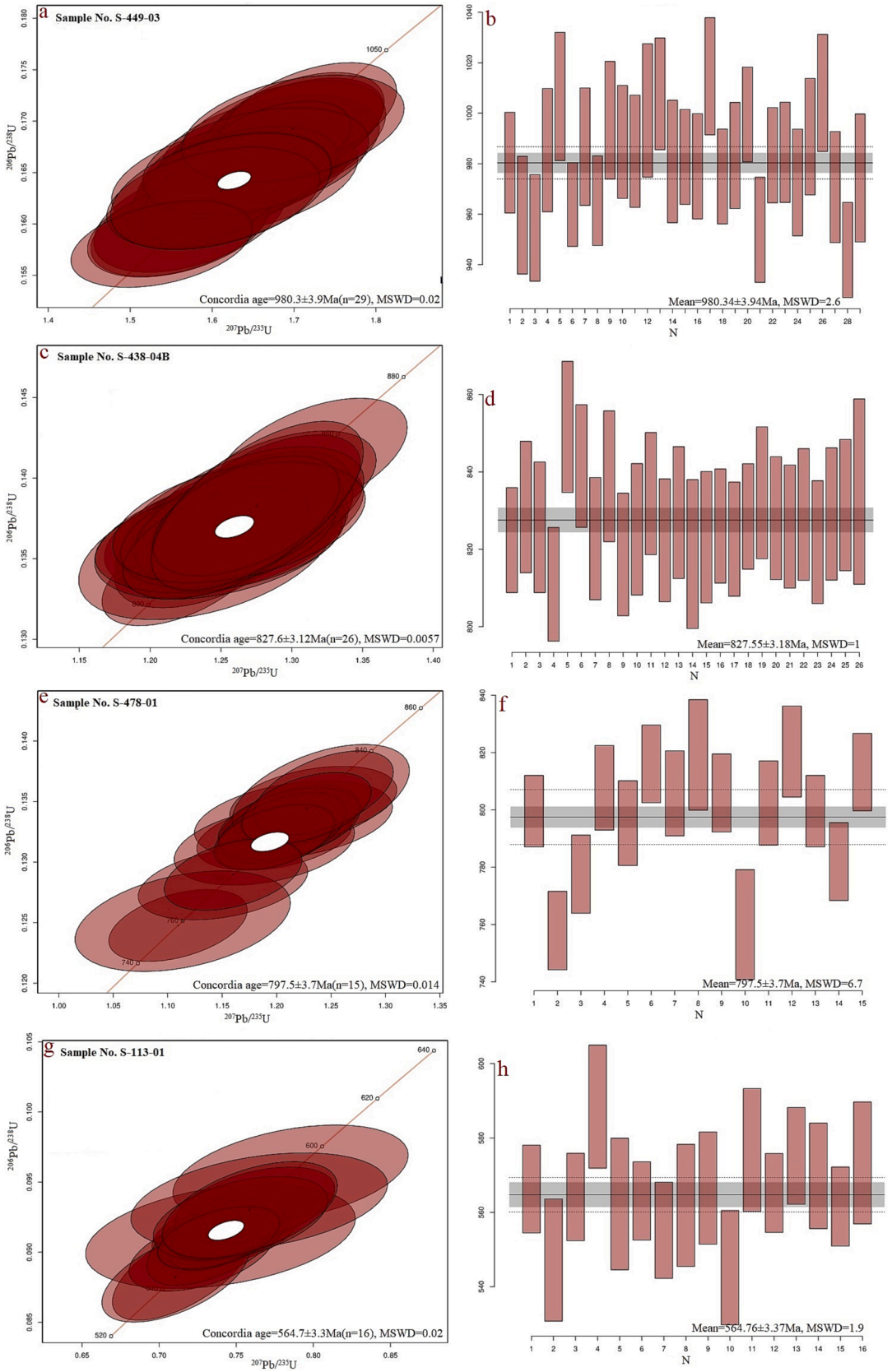

Fig. 4. Cathodoluminescence (CL) images for representative zircons from (a) calc-alkalic granitoid (S-478–01); (b) alkali-calcic granitoid (S-113–01); (c) meta-granitoid (S-449–03) and (d) calcic granitoid (S-438-04B) in the Gimbi-Nejo area. Circles indicate locations of LA-ICPMS analyses (Red circles for U-Pb isotopic analyses & yellow circles for Lu-Hf isotopic analyses).

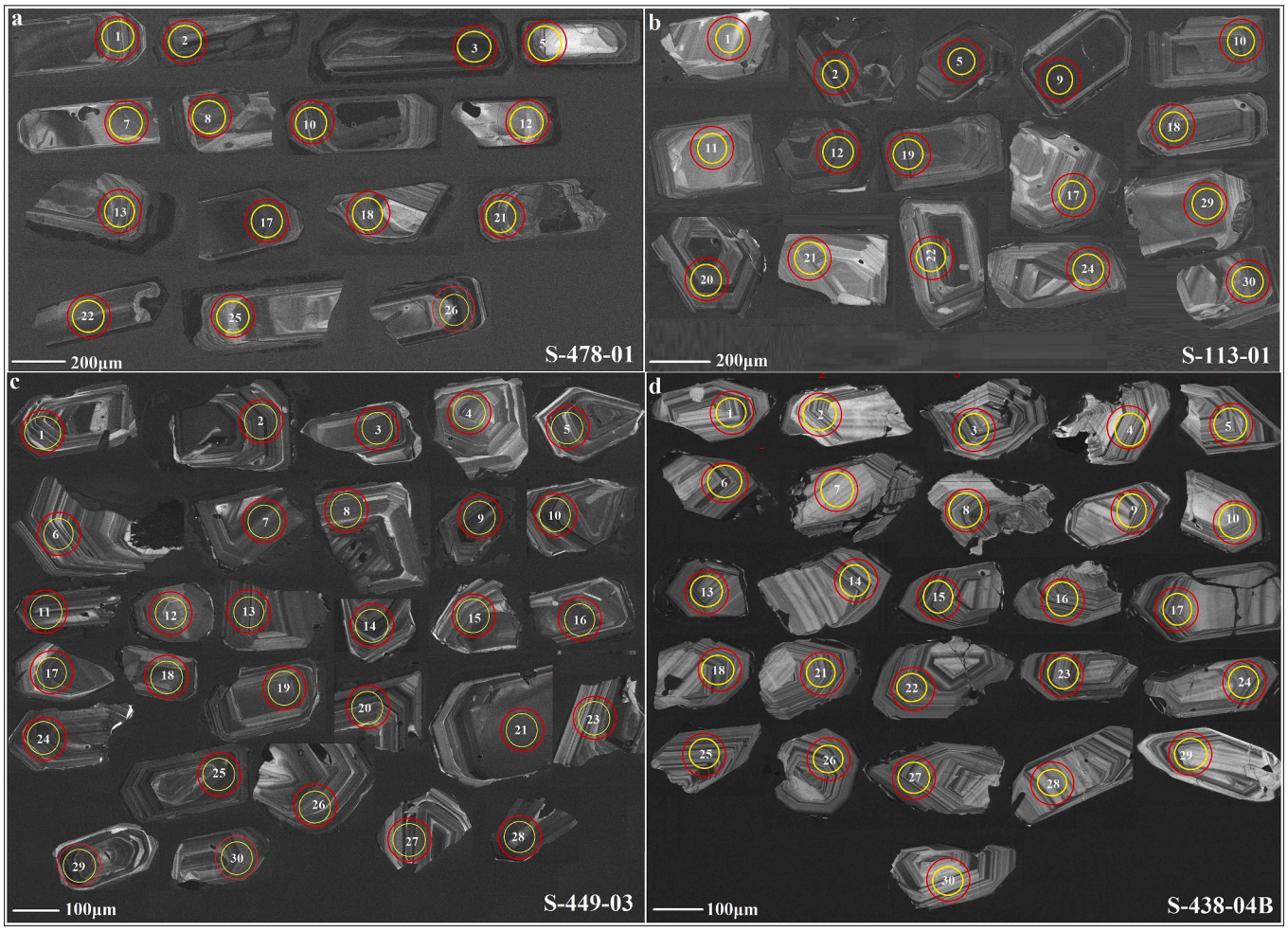

Fig. 5. U-Pb Concordia diagrams and weighted mean ages of zircon grains from (a, b) met-granitoid (S-449–03); (c, d) calcic granitoid (S-438-04B); (e, f) calc-alkalic granitoid (S-478–01); (g, h) alkali-calcic granitoid (S-113–01) sample.

samples show enrichment of U, K, Pb, Nd, Li, Hf, and depletion of Ba, Nb, Ta, La, Ce, Sr, P, Zr, Ti, and Eu, and alkali-calcic granitoid samples show enrichment of U, Ta, Pb, Eu, Nd, and depletion of Rb, Ba, Th, Nb, La, Ce, Sr, P, Zr, Hf, Ti, Li, Y (Fig. 8).

5. Discussion

5.1. Alteration effects

In this study, different types of magmatic rock samples were used to review the Neoproterozoic Pan-African basement of West Ethiopia. The intrusive rock samples exhibit a lower, variable degree of alteration than the metamorphosed intrusive rock samples (see Tables 1 & 2 of supplementary material). The relatively fresh/minor altered rock samples have LOI values less than 3 wt%, while highly altered samples have LOI values greater than 4 wt% (Tatsumi and Eggins, 1995; Kraus, 2005; Wang et al., 2009). The intrusive rock samples, including pyroxenite, gabbro, and granitoid, have LOI values of 1.18 wt%, 0.04–2.04 wt% (except for sample S-041–01, with a value of 8.42 wt%), and 0.02–2.87 wt%, respectively. Similarly, *meta*-intrusive rock samples, including *meta*-peridotite, *meta*-gabbro, and *meta*-granitoid, also have LOI values of 4.4–27.4 wt%, 0.6–5.8 wt%, and 0.2–0.9 wt% (S-GB-12: LOI = 3.95 wt%), respectively. These rocks from the *meta*-ultramafic show high loss on ignition values, suggesting high water contents and appearing different from the patterns shown in several diagrams. Under these conditions, alkali major elements and large ion lithophile elements (LILE) are especially vulnerable to alteration (Rollinson, 1993). Alkali discrimination plots involving norm calculations have been avoided in the following analysis due to the possibility of alkali migration. According to the criteria set by Polat and Hofmann (2003) and Polat et al. (2002), the metamorphosed gabbro samples in this study, characterized by LOI values < 6 and moderate Ce anomalies with Ce/Ce* ratios of 0.04–0.2, are considered least altered. For more accurate results, utilize selective elements such as Hf, Ta, La, Sm, Nb, Yb, and Th to discriminate the tectonic setting. These elements exhibit a better correlation with Zr (Manikyamba et al., 2021) content but do not correlate with LOI (Cai et al., 2023), indicating their resistance to mobilization (see Fig. 6).

5.2. Revised Neoproterozoic geochronology

The Neoproterozoic era, which spanned from approximately 1 billion years to 541 million years ago (Gradstein et al., 2018), is a significant period in Earth's history characterized by the formation of the supercontinent Rodinia (Hoffman, 1991; Zhao et al., 2002; Li et al., 2019). Revised Neoproterozoic geochronology data has been obtained through a variety of methods, including radiometric dating of minerals such as zircon and monazite, as well as paleomagnetic studies. These studies have allowed for a more accurate determination of the ages of the various tectonic events that occurred during the Neoproterozoic era. The exact Neoproterozoic era continental rifting, subduction, collision, and strike-slippage ages proposed by different authors can vary, as there is ongoing research and debate on the topic. Table 1 presents some of the prominent Neoproterozoic ages proposed by different authors in the 21st century, based on geological and geochronological evidence from

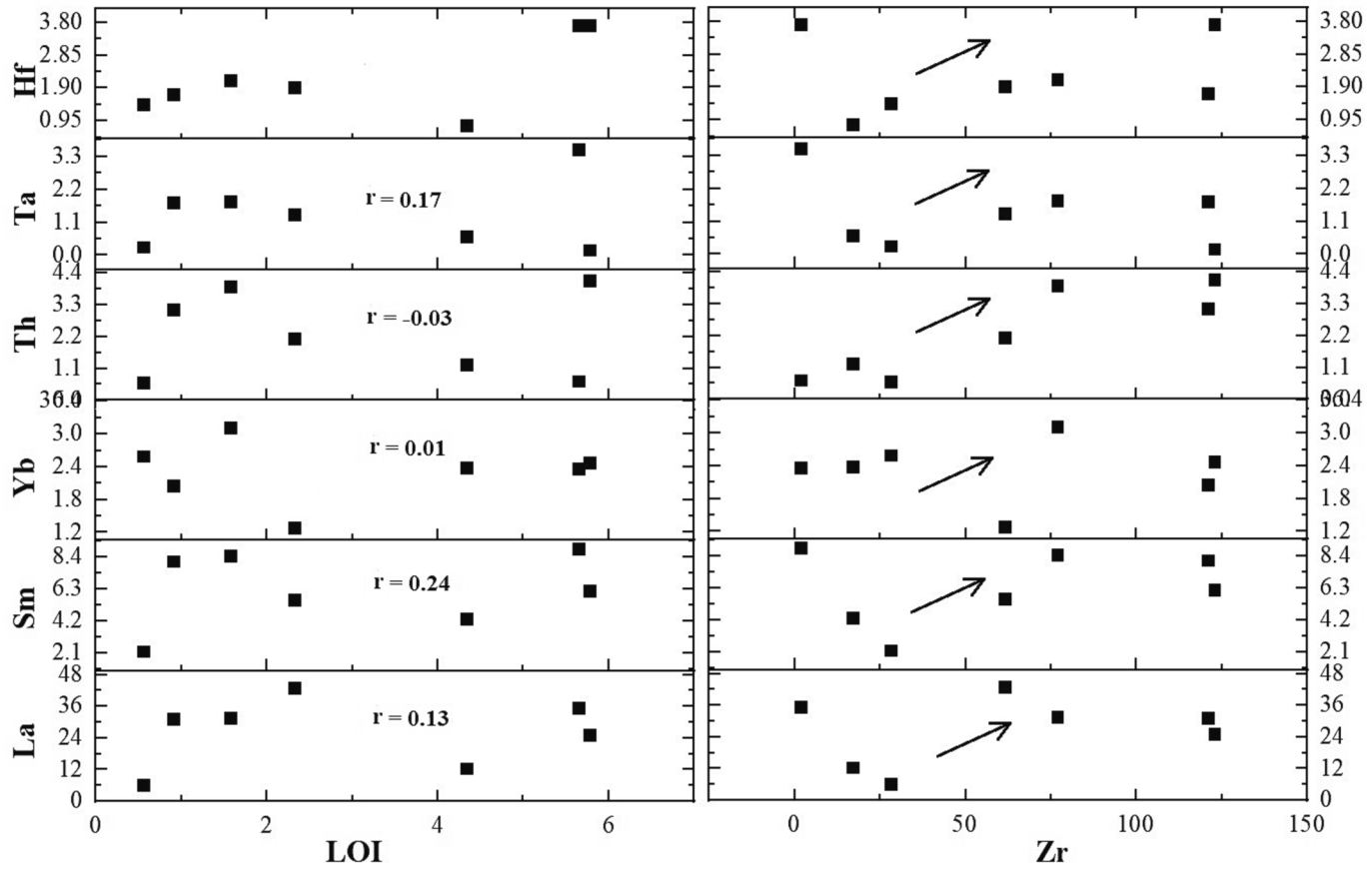

Fig. 6. Plot showing meta-gabbro samples with HFSE (Th, Ta, Hf) & REE (La, Sm, Yb) contents correlated with LOI & Zr contents. The Pearson correlation coefficient (r) is negligible within the range of + 0.3 to −0.3. In other words, LOI contents do not have a correlation with elements.

different parts of the world. Among these ages, the rifting age of Rodinia 980 Ma, which was collected from *meta*-granitoid of Pan-African basement, west Ethiopia, is the oldest one probably till discovered. The subduction ages of the Neoproterozoic oceanic lithosphere proposed by various authors in the Pan-African basement rocks range from 955 to 608 Ma. However, this study reports a lithospheric subduction age of 827 Ma based on the analysis of Pan-African calcic granitoid. The Neoproterozoic ages of continental collisions resulting in the formation of the Pan-African orogeny and characterized by sinistral ductile shearing deformation, as proposed by various authors, range from 670 to 500 Ma and 639 to 493 Ma, respectively. In this study, a collisional age of 797 Ma and a sinistral ductile shearing deformation age of 564 Ma were determined based on the analysis of Pan-African calc-alkalic granitoid and alkali-calcic granitoid, respectively. The short time gap of 30 million years between subduction and collision suggests an early stage of continental collision, with the subduction process being in its final stage.

5.3. Geochemical characteristics of intrusive and meta- intrusive rocks

The meta-intrusive basement rocks of the Gimbi-Nejo area comprise mainly talc-schist, serpentinized dunite, pyroxenite, felsic schist, migmatitic biotite gneiss, orthogneiss, quartzite, plagioclase amphibolite, greenschist, and chloritized epidotized felsic schist. Regarding their geochemistry, the metamorphosed peridotite and gabbro samples display a tendency towards the tholeiite series, while the meta-granitoids tend to exhibit a trend towards the calc-alkaline series in the AFM-plot (Fig. 7a, b).

The elemental and isotopic composition of igneous rocks can be affected by crustal contamination (DePaolo, 1981). Rocks from the mantle that have been contaminated by the crust may exhibit an enrichment in crustal elements. The meta-gabbro rock samples of this study are minorly contaminated, resulting in depletion in Nb and Zr anomalies with enrichment in Pb, Ba, and Cs relative to other elements in spider diagrams (Fig. 8). The presence of negative to positive Eu anomalies in the *meta*-gabbro also suggests that minor contamination has occurred.

The source region of mantle-originated rocks could be examined by rare earth elements compatibility (Jenner et al., 1993). In the plots of Sm/Yb vs. La/Yb, meta-gabbro rock samples are trending from garnet to garnet-spinel lherzolite zone with degrees of partial melting 2–40 %, while samples of meta-peridotite rocks are trending from garnet-spinel lherzolite to spinel lherzolite with degrees of partial melting < 10 % (Fig. 11).For more clarification about the source region of metamorphosed intrusive rocks of this study, Lu-Hf isotopic analysis was also performed on the twenty-nine magmatic zircon grains of meta-granitoid (S-449–03). This sample is enriched in alkalies and silica (Fig. 8), probably a result of magmatic differentiation or crustal material. The isotopic ratios are homogenous with a positive value of εHf (t) + 9.4 to + 15.5 (Table 7 of supplementary material). The Hf isotopic composition of meta-granitoid's detrital zircon grains suggests their magma is generated from the juvenile crust, (Fig. 10) same as Mozambique belt (Manda et al., 2019). Its two-stage modal age TDM2 (949–1233 Ma) indicates the protolithic material extraction time from Depleted mantle source. A shorter difference between the zircon crystallization age ($^{206}Pb/^{238}U$) and the model age (TDM2) suggests that granitoids were derived from crustal materials that formed through the partial melting of the depleted mantle, which (depleted mantle source) ascended to the paleo crust and remained there for a certain period (mean time = 122 Ma). The same phenomenon has also been observed in Sugensala granite in the western Junggar, by Song et al. (2022). The distribution pattern of these meta-granitoids is similar to A-type granitoids. In the Ce/Nb vs. Y/

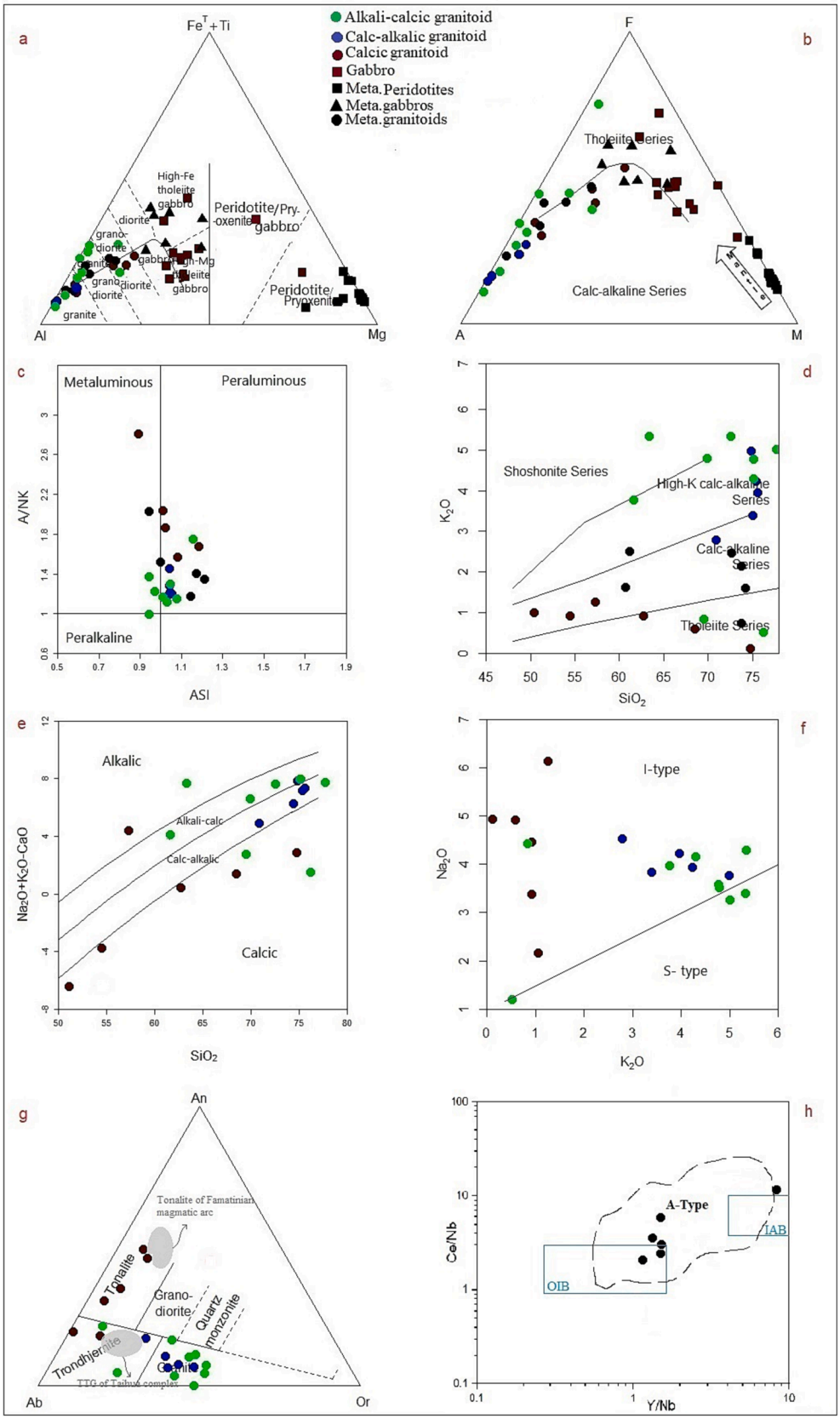

Fig. 7. Plots for the intrusive and metamorphosed intrusive rocks of the Gimbi-Nejo, west Ethiopian plateau: (a) Al - Mg - (Fe^T + Ti) (after Jensen, 1976); (b) AFM (after Irvine and Baragar, 1971); (c) A/NK vs. ASI (Frost et al., (2001); (d) SiO_2 (wt.%) vs. K_2O(wt.%) (after Peccerillo and Taylor, 1976); (e) SiO_2 (wt.%) vs. $Na_2O + K_2O - CaO$ (wt.%) (after Frost et al., 2001); (f) Na_2O (wt.%) vs. K_2O (wt.%) (after Amam, 2001; Lissan and Bakheit, 2011; Jam et al., 2022); (g) Feldspar triangle showing the TTG samples (after O'Conner, 1965), shadow zone from Wang et al., 2016 and Otamendi et al., 2009; (h) Ce/Nb vs. Y/Nb plot for A-type granite (modified after Eby, 1992).

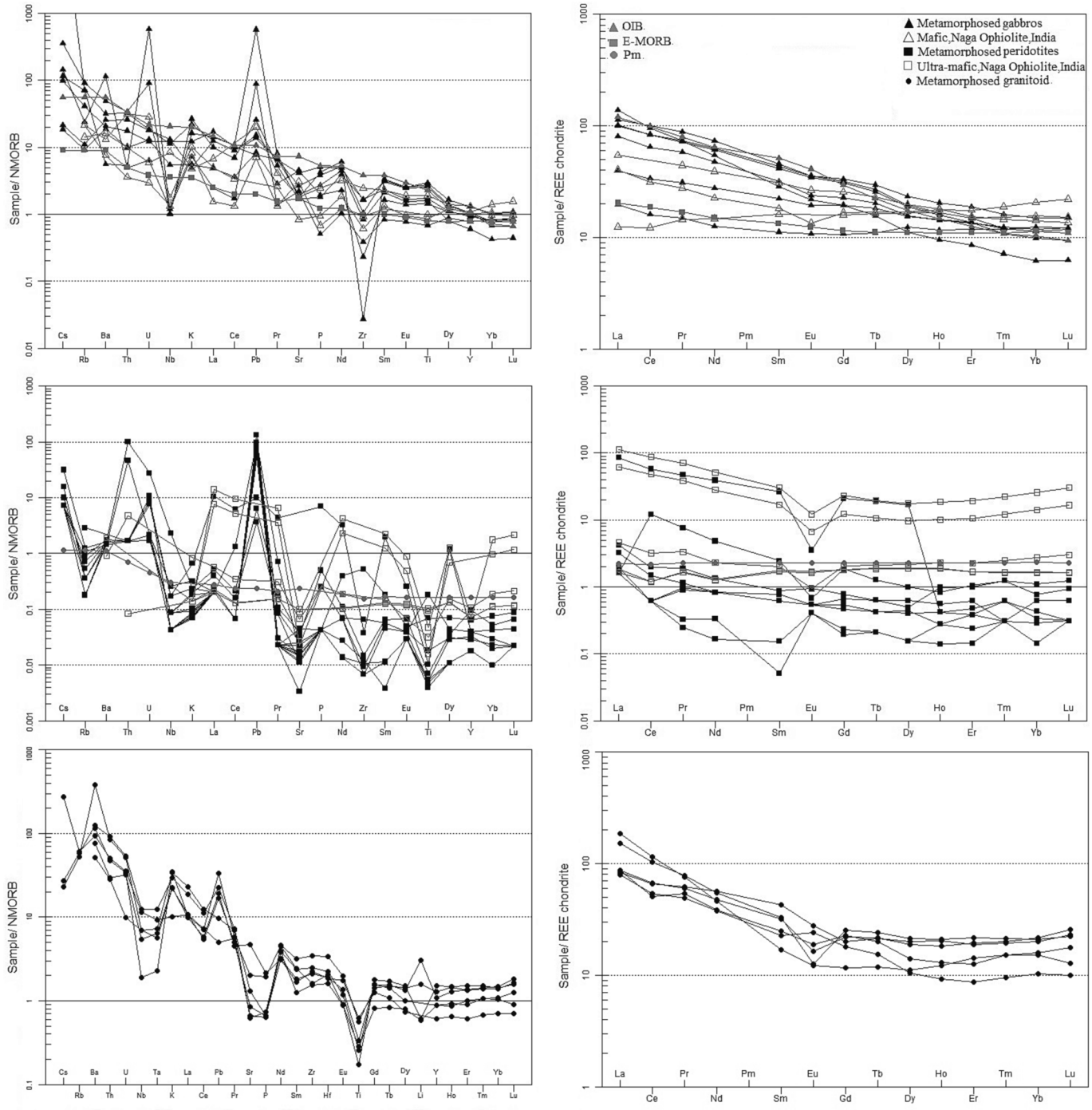

Fig. 8. Primitive mantle-normalized trace elements and chondrite-normalized rare earth elements (REE) spider diagrams for the metamorphosed intrusive rocks of the west Ethiopian plateau. Mantle-normalization values are from Sun and McDonough (1989). REE normalizing values are from Boyton (1984). Naga ophiolitic mafic and ultramafic samples (Dey et al., 2018); Pm, OIB, and E-MORB samples (Sun and McDonough, 1989) are used for comparison.

Nb plot, these meta-granitoids are in A-type granitoid zone (Fig. 7h).

The intrusive basement rocks of the Gimbi-Nejo area comprise mainly pyroxene bearing gabbro, olivine gabbro, talcose gabbro, hornblendite inclusion in diorite, tonalite, trondhjemite, granite, alkali granite, granodiorite, quartz syenite, and quartz monzonite. The gabbro samples found among these intrusive rocks belong to the tholeiite series, while the granitoids are classified as being part of the calc-alkaline series (Fig. 7a, b). Tholeiitic gabbro samples show depletion in Nb and Ta anomalies with enrichment in Cs, Ba, Sr, and Pb anomalies in the spider diagram, indicating crustal contaminations but minor due to depletion of Zr and Hf with enrichment of Eu (Fig. 9). For the source region, gabbro samples in the plot of Sm/Yb vs. La/Yb are trending from garnet lherzolite to garnet-spinel lherzolite with degrees of partial melting < 30 % (Fig. 11c).

The granitoids are the best tool for studying the geochemical evolution of the continental crust, particularly with regard to their isotopic analyses which exhibit the mantle and crust contribution (Kebede et al., 1999). In this study, granitoid samples were collected from three different localities in the field based on regional deformation features, and were therefore geochemically divided into calc-granitoid (Na_2O + K_2O – CaO = 4.4 to −5.9 wt%), calc-alkalic granitoid (Na_2O + K_2O – CaO = 7.8 to 4.9 wt%), and alkali-calcic granitoid (Na_2O + K_2O – CaO =

Table 1
The prominent Neoproterozoic tectonic stage ages proposed by different authors in the 21st century.

Continental rifting stage			Lithospheric subduction stage			Continental rifting stage			Strike-Slippage stage		
Age (Ma)	Locality	Authors	Age (Ma)	Locality	Authors	Age (Ma)	Locality	Authors	Age (Ma)	Locality	Authors
742	SW-America	Karlstrom et al., 2000	625–653	Tanzania	Moller et al., 2000	628	Brazil	Hackspacher et al., 2000	571	Brazil	Hartmann et al., 2002
803	South China	Li, 2001	850–770	East Ethiopia	Tadesse et al., 2000	633	Brazil	Hartmann et al., 2002	579	Brazil	Silva et al., 2003
850–900	Scandinavian	Paulsson, 2002	780–700	Western Ethiopia	Kebede et al., 2001	628	Brazil	Silva et al., 2003	533	Brazil	Prazeres Filho, 2005
830–820	South China	Jian and Li, 2003	743	Moroccan	Thomas et al., 2002	620	Brazil	Tassinari et al., 2004	529	Brazil	Basei et al., 2008
723	Canada	Shellnutt et al., 2004	699	Western Ethiopia	Grenne et al., 2003	627	Brazil	Prazeres Filho, 2005	530	Brazil	Petitgirard et al., 2009
827-777	China	Wu, 2005	798	Western Ethiopia	Johnson et al., 2004	591	Brazil	Noce et al., 2007	493	Brazil	Bento dos Santos et al., 2010
774	Argentina	Baldo et al., 2006	762	Moroccan	Samson et al., 2004	630	Brazil	Borba et al., 2008	500	Brazil	Azevedo Sobrinho et al., 2011
830–740	NW China	Zhang et al., 2007	776	Western Ethiopia	Kebede et al., 2007	641	Brazil	Siga et al., 2009	587	Brazil	Chemale et al., 2012
825	South China	Wang et al., 2008	846-856	Western Ethiopia	Woldemichael and Kimura 2008	595	Brazil	Novo et al., 2010	580	West-Cameroon	Kwékam et al., 2013
746 ~ 827	South China	Xu, 2009	955–845	Kenya–Tanzania	Bauernhofer et al., 2009	597	Brazil	Pedrosa-Soares et al., 2011	504	Brazil	Gradim et al., 2014
860–830	Western Ethiopia	Woldemichael et al., 2010	778	Western Ethiopia	Woldemichael et al., 2010	646	Brazil	Chemale et al., 2012	560-490	SE Brazil & Uruguay	Telmo et al., 2015
700-650	Australia	David and Greene, 2010	608	South-Togo	Ganade de Araujo et al., 2014	664	Brazil	Alves et al., 2013	580	Chad	Shellnutt et al., 2017
800	NW China	Liangshu et al., 2011	740–720	Moroccan	Antoine et al., 2015	587	Brazil	Gradim et al., 2014	635-639	Western Ethiopia	Bowden et al., 2019
750–850	America	Christopher et al., 2012	800–780	Mali	Stéphane et al., 2018	670-595	SE Brazil & Uruguay	Telmo et al., 2015	564	West Ethiopia	This study, 2023
720	America	Elizabeth et al., 2013	850	Eritrea	Fitwi et al., 2019	600-650	Chad	Shellnutt et al., 2017			
760–750	North America	Elizabeth and Esteban, 2014	797	Western Ethiopia	Bowden et al., 2019	500	southern India	Joy et al., 2018			
800-810	South China	Xiaozhuang et al., 2015	893-767	S. China	Yiming et al., 2021	797	West Ethiopia	This study, 2023			
743–711	central China	Ruibao et al., 2016	827	West Ethiopia	This study, 2023						
820–785	Africa	Jiří et al., 2017									
850–550	East European Craton	Piotr et al., 2018									
800	S. China	Jiawei et al., 2019									
750	NW America	Daniel et al., 2020									
800		David, 2021									
980	West Ethiopia	This study, 2023									

8 to 1.5 wt%; Fig. 7b). All of these granitoid samples are peraluminous I-type except for the alkali-calcic granitoids, which are peraluminous-metaluminous and trending from S-type to I-type in the K_2O vs. Na_2O plot (Fig. 7f). The West Ethiopian Assosa granites are also metaluminous-peraluminous in nature (Kebede et al., 2000). Field mapping revealed that mafic rock is in contact with both alkali-calcic and calc-alkalic granitoids (as in the Dega Bor area), but in most localities of alkali-calcic granitoids, there was no mafic magma signature. This suggests that the granitoids may have originated from the lower continental crust, influenced by fluids related to subduction. The enrichment of U in calc-alkalic granitoids, U and Cs in calc- and alkali-calcic granitoids, and depletion of Nb, Ta, P, and Ti in all granitoids are characteristic of the continental crust, resulting from differentiation of magmas (Fig. 8; Taylor and McLennan, 1995). Low-medium K tholeiitic calcic granitoid trends in the tonalite and trondhjemite zones of the ternary plot (Fig. 7g). Calc-granitoid samples also have trace and rare earth elements partition patterns similar to those of the TTG of the Famatinian magmatic arc in Argentina, as shown in the spider diagrams (Fig. 9).

Lu-Hf isotopic analysis of igneous rocks is a tool to distinguish source areas (Wu et al., 2006). The Lu-Hf isotopic analysis of twenty-six calcic-granitoid (S-438-04B), fifteen calc-alkalic granitoid (S-478-01), and sixteen alkali-calcic granitoid (S-113-01) zircon grains exhibits positive homogenous values of εHf (t) + 7.6 to + 13.2, +7.4 to + 15.5, and + 7.1 to + 17.1, respectively (Table 8–10 of supplementary data). This calcic-granitoid sample, with a low $Na_2O + K_2O$ (5.51 wt%) value, is probably the product of mixing mafic and crustal material (Bas et al., 1986).

The isotopic characteristics suggest granitoid magma originated

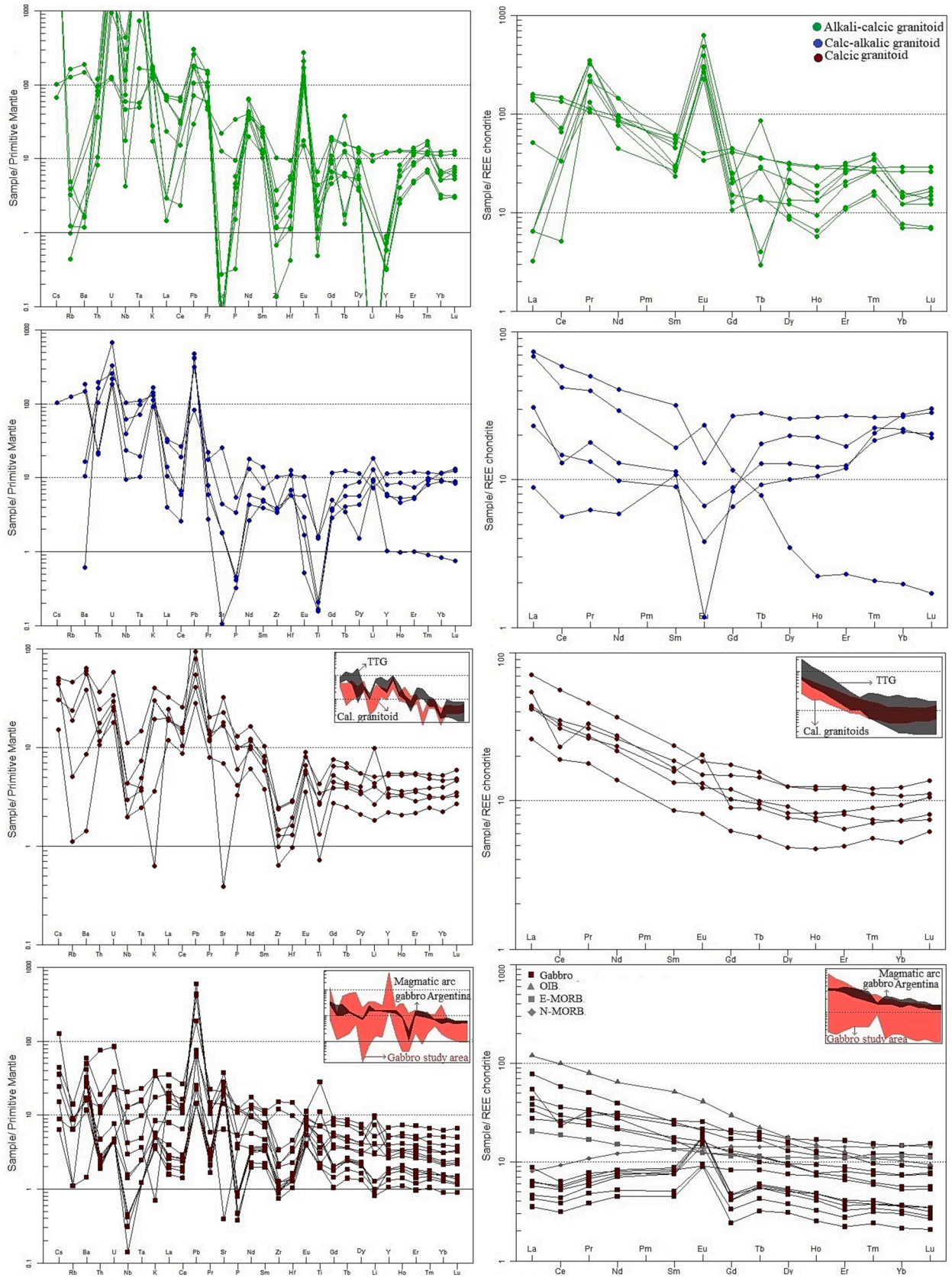

Fig. 9. Primitive mantle-normalized trace elements and chondrite-normalized rare earth elements (REE) spider diagrams for the intrusive rocks of the west Ethiopian plateau. Mantle-normalization values are from Sun and McDonough (1989). REE normalizing values are from Boyton (1984). Magmatic arc gabbro from Otamendi et al. (2009), and TTG from Otamendi et al. (2009) & Wang et al. (2016) are used for comparison; OIB, N-MORB, and E-MORB samples (Sun and McDonough, 1989) are used for comparison.

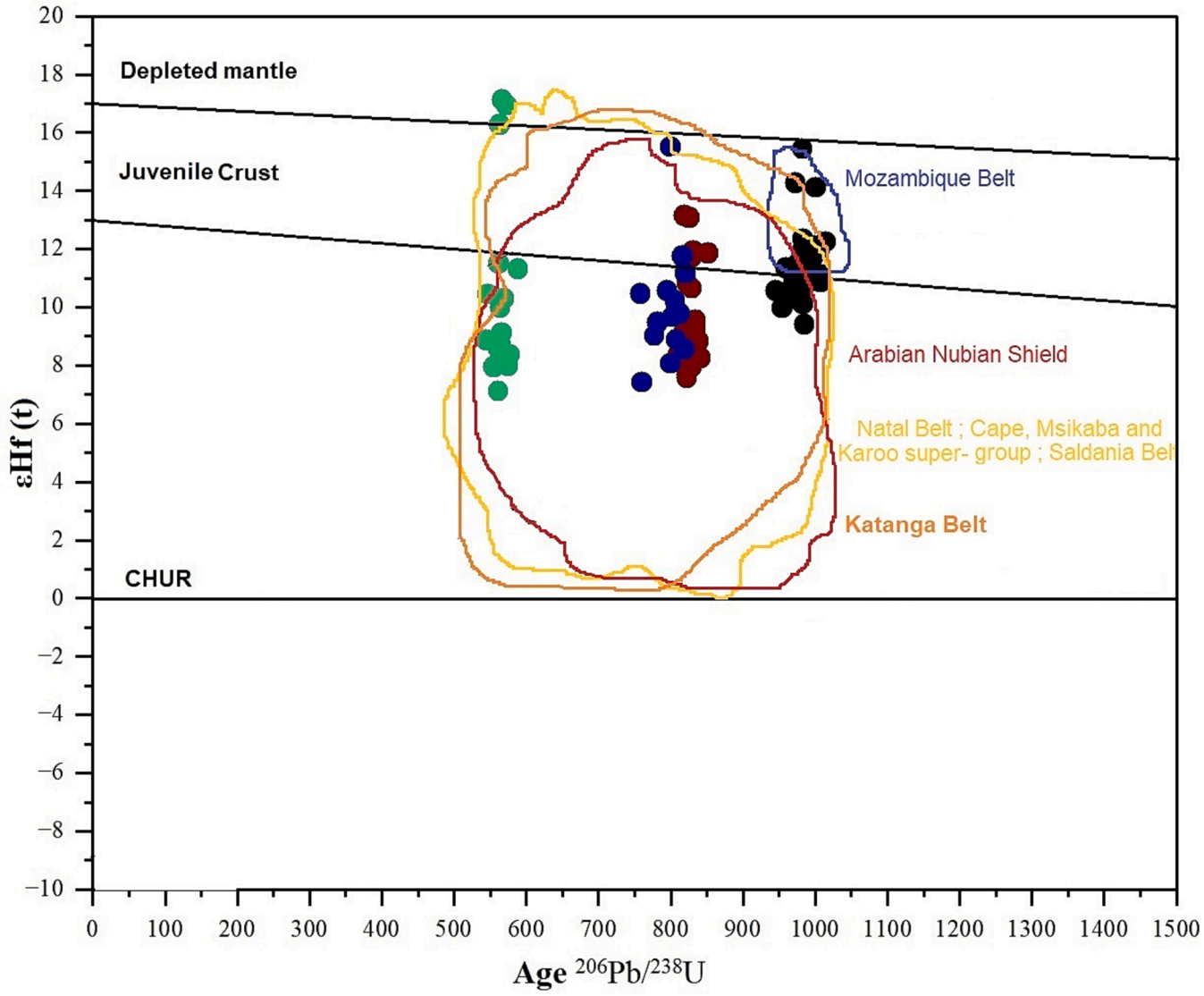

Fig. 10. Plot of εHf (t) vs. U-Pb age for met-granitoid (S-449–03), calc-granitoid (S-438-04B), calc-alkalic granitoid (S-478–01), and alkali-calcic granitoid (S-113–01) sample. Comparison of zircon Hf isotope-age data obtained from Arabian Nubian Shield (Be'eri-Shlevin et al., 2009; Morag et al., 2011; Ali et al., 2016); Natal Belt (Kristoffersen et al., 2016); the Cape, Msikaba and Karoo super-groups (Andersen et al., 2016); the Saldania Belt (Frimmel et al., 2013); Mozambique Belt (Manda et al., 2019); Katanga Belt (Batumike et al., 2007). Nearly perfect circles of comparison data are direct evidence of partial melting of crustal material during Proterozoic eon. The ranges for depleted mantle (DM), chondritic uniform reservoir (CHUR), and juvenile crust from Griffin et al. (2004) and Yuan et al., (2020). The symbols are the same as in Fig. 7.

from the partial melting of the juvenile crust. The juvenile crust originated from depleted mantle source (Vervoort and Kemp, 2016). It is supported by age (Ma) vs. εHf (t) plot, in which zircon grains of all three granitoid samples are trending toward juvenile crust (Fig. 10). Lu-Hf studies of Arabian Nubian Shield (Be'eri-Shlevin et al., 2009; Morag et al., 2011; Ali et al., 2016); Natal Belt (Kristoffersen et al., 2016); the Cape, Msikaba and Karoo super-groups (Andersen et al., 2016); the Saldania Belt (Frimmel et al., 2013); and Katanga Belt (Batumike et al., 2007) have also shown that these rocks were derived from juvenile crust during Proterozoic eon. The two-stage model age (TDM2) suggests that calcic-, calc-alkalic, and alkali-calcic granitoids source crustal material (juvenile crust) formed during 1220–863 Ma, 1181–698 Ma, and 1043–408 Ma respectively, from depleted mantle (DM) source. Which (DM-magma) rose to the paleo crustal material and remained there for a certain period (mean time = 257 Ma, 248 Ma, and 256 Ma respectively). Few zircon grains of alkali-calcic granitoid are trending toward depleted mantle in the plot (Fig. 10), indicated that source material was probably heterogeneous.

5.4. Tectonic implications

The PAO is a product of the tectonic evolutionary cycle of the plates, which occurred 550 million years ago (Stern, 1994). The evidence for this is a series of ophiolites in the ANS and the MB. According to the preceding viewpoint, the Gimbi-Nejo area has undergone four distinct tectonic stages, as observed during the field survey.

The continental rifting stage in the area is suggested by the association of meta-clastic rocks (Fig. 2f), calcic-silicate rocks, and meta-mafic rocks bearing marble (Fig. 2i) in the Chochi and Kata domains, consistent with sedimentary formations of rift valleys. Similar meta-sedimentary deposits of rifting are present in Sudan (Kröner et al., 1987) and Kenya (Mosley, 1993). These areas also contain a bimodal volcanic (lack of real andesite) association of metamorphosed mafic and granitoid rocks (Fig. 2a) overlain by quartzite, mica schist, phyllite, graphite schist, and marble in the Sayi Chenga group. Hanson et al. (1994) suggested that this type of bimodal volcanic overlain by sediments and marine carbonate rock indicates sea-floor spreading and

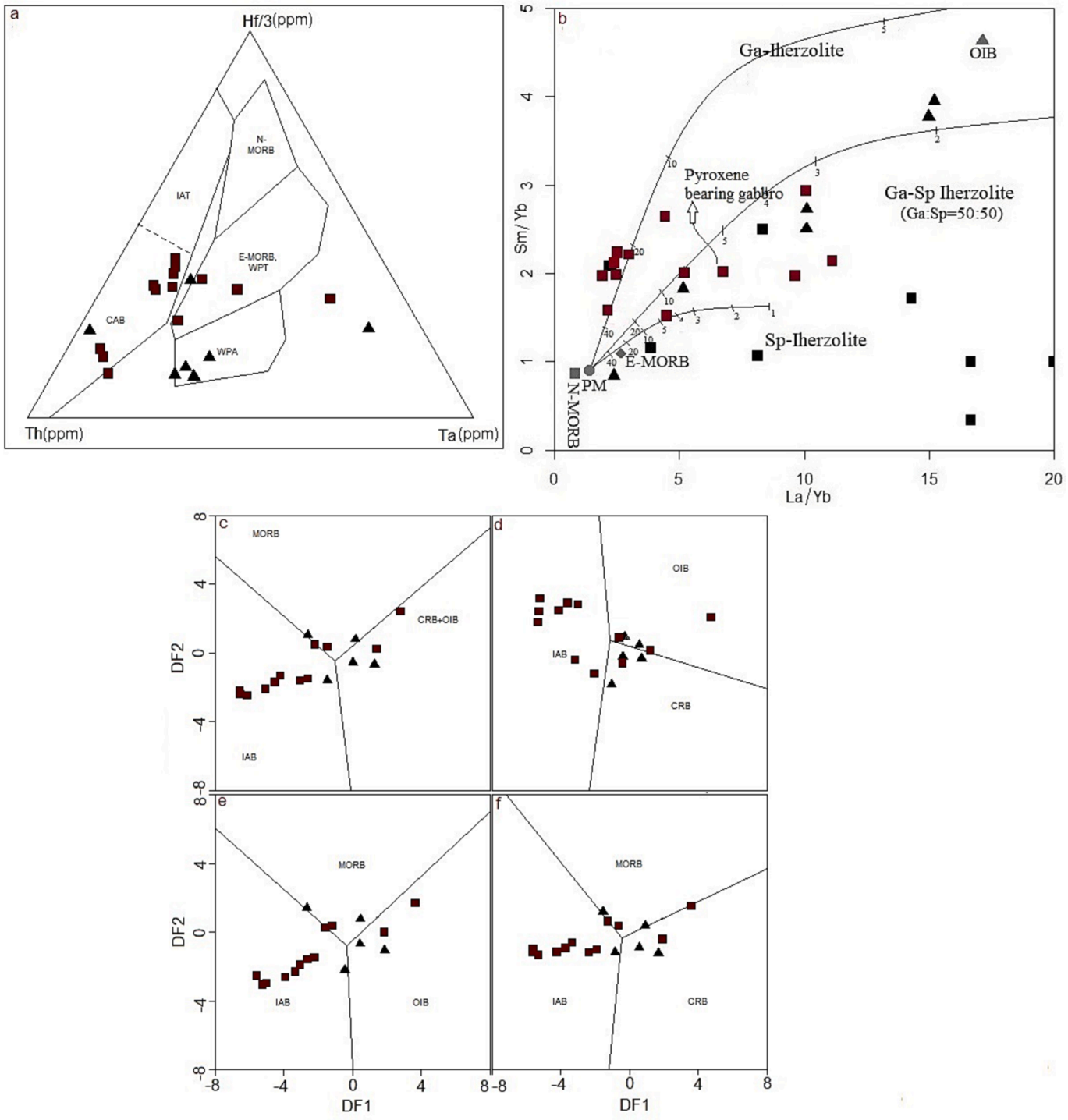

Fig. 11. (a) Tectonic discrimination diagram Th – Hf/3 – Ta (Wood, 1980); (b) Sm/Yb vs. La/Yb plot (after Aldanmaz et al., 2000; Zhao and Zhou, 2009) showing partial melting of meta. Peridotite and Gabbro - meta. Gabbro from the garnet lherzolite to spinel lherzolite mantle zone. Mantle array is defined by a depleted MORB mantle (McKenzie and O'nions, 1991) and primitive mantle (PM) (Sun and McDonough, 1989). Melting curves for spinel lherzolite ($Ol_{53} + Opx_{27} + Cpx_{17} + Sp_{11}$) and garnet peridotite ($Ol_{60} + Opx_{20} + Cpx_{10} + Gt_{10}$) with PM compositions are after Aldanmaz et al. (2000). Numbers along lines represent the degree of the partial melting; (c, d, e, f) Discrimination of geotectonic environment of gabbro, proposed by Agrawal et al. (2008). It is based on log-transformed concentration ratios of five immobile elements (La, Sm, Yb, Nb, and Th), i.e., using four ratios ln (La/Th), ln (Sm/Th), ln (Yb/Th), and ln (Nb/Th). The symbols are the same as in Fig. 7.

rifting stage. Near the Hagelometi area, serpentinized kazanskite, green schists, and sheets of silicolites can be observed together as a rock assemblage with contact along faults. It is identified as an ophiolite. Tadesse and Allen (2005) have also classified ultramafic slices from the Sayi Chenga group as a part of ophiolites derived from the oceanic crust. The Sayi Chenga group structurally overlies the Tulu Dimtu belt to the west. In the Tulu Dimtu tectonic mélange belt, the greenschist cuts through serpentinite, which can be observed in the Gidano Kingi area. The dyke greenschist's original rock is diabase (Fig. 2c) and its rock assemblage is similar to ophiolite. In some places, such as Chabi valley and the Hagelo Meti area, the greenschist shows pillow structures (Fig. 2d). Both ophiolite tectonic slice and bimodal volcanic rock

tectonic slice with deep-sea turbidity current deposits (Fig. 2e) in the Sayi Chenga group (Psmv), indicating the existence of a tectonic mélange in this mapping unit. These are direct evidence of the existence of a paleo-oceanic crust (856.3 ± 9.8 and 846.0 ± 7.6 Ma; Woldemichael et al., 2009). The distribution pattern of trace and rare earth elements in *meta*-peridotite and *meta*-gabbro rocks on spider plots is similar to ultramafic and mafic rocks of the Naga Hills ophiolite, India (Fig. 8). In the discrimination ternary plot (Th – Hf/3 – Ta), meta-gabbro samples trend from within-plate alkaline basalt (WPA) toward enriched mid-oceanic ridge basalt (E-MORB) and within-plate tholeiitic basalt (WPT) (Fig. 11a). In all DF1-DF2 plots, meta-gabbro samples generally trend from oceanic island basalt (OIB) and continental rifting basalt (CRB) toward mid-oceanic ridge basalt (Fig. 11c-f). Meta-granitoids of the study area are A-type granitoids (Ce/Nb 2.1–11.9; Y/Nb 1.2–8; Yb/Ta 2.6–14), associated with extensional stages (Eby, 1992; Fitwi et al., 2019). In the discrimination diagrams, these are trending towards within-plate granite (Fig. 12b-e).

In the study area, the ocean floor subduction stage experience area is represented by a magmatic arc composed of gabbros and granitoids. The contact between pyroxenite and gabbro in the Gori area could be considered as ophiolitic fragments. The fore-arc basin of PAO contains ophiolitic boninites (Rahman, 1993). In the spider diagrams, the trace and rare earth elements partition pattern of gabbros along E-MORB is similar to magmatic arc gabbros of Argentina (Fig. 9). In the discrimination ternary plot (Th – Hf/3 – Ta), gabbro samples are present within continental arc basalt zone (Fig. 11a), and in the DF1-DF2 plots, these rock samples are present inside island arc basalt zone (Fig. 11c-f). Tonalite and trondhjemite samples in the discrimination diagrams are present within volcanic arc granite field (Fig. 12b-e). The tonalite and trondhjemite samples with high Sr/Y (14.2–48.2) ratios indicate adakitic characteristics. Their Y (10–24.8 ppm) and Yb (1.1–2.6 ppm) values change inversely with SiO_2 (53.8–74.8 wt%) like Cenozoic adakitic rocks around the Pacific Ocean and Neoproterozoic adakitic rocks in ANS (Richards and Kerrich, 2007), thus proving that this area was involved in plate subduction. The continental collision stage is characterized by N-S thrust-folds belt associated with intermediate-acid intrusive rocks distributed on Chochi, Giranche, Borchica, and Kalisi orogeny, and regional greenschist facies-low amphibolite facies metamorphism (Fig. 2g, i). The tectonic hydrothermal activities along this N-S structural belt have the dominant control function for regional mineralization (Junaid et al., 2022). The crustal shortening stage is represented by NW sinistral ductile shear deformation that has reformed the thrust-folds within the Tulu Dimtu tectonic belt and Chochi shear zone. The decollement is the dominant deformation in this post-stage area with small-scale folds of the early stage associated with leucocratic granites.

The virgin calc-alkalic granitoid samples, which were collected from the vicinity of the N-S trending suture zone fall in the "within the plate granite" field, while alkali-calcic granitoid samples of the NW strike-slippage area are trending from "within the plate granite" to "volcanic arc granite" field (Fig. 12b-e). In R1 vs. R2 plot, calc-alkalic granitoid samples are present in the surrounding of the syn-collision zone, while alkali-calcic granitoid samples are trending from late to post-orogenic zone (Fig. 12a). Post-collisional granites would be present along belts that bisect the crust in the west Ethiopian plateau (Barbarin, 1999). These within-plate granite signatures suggest that probably melted sediments of calc-alkalic granitoid magma eroded from mafic rocks of mid-ocean ridges or were previously settled with meta-sediments within the continental crust melted by crustal thrusting and thickening. Similarly, volcanic arcs and within-plate granite signatures of granitoid samples suggest that probably melted sediments of alkali-calcic granitoid eroded from mid-ocean ridges and island arcs or were previously settled with meta-sediments within the continental crust melted by sinistral ductile shearing deformation. Alkali-calcic granitoids with metaluminous-peraluminous features also indicate that the continental crust origin probably has experienced continent collision or subduction (Kebede et al., 2000). West Ethiopian Assosa granites with enrichment of incompatible elements also suggest the contribution of meta-sediments (Soltani, 2000). In spider diagrams, the positive-to-negative Eu anomaly of both types of granitoids also represents magma derived from various provenances (Fig. 9).

In conclusion, the west Ethiopian Pan-African basement rocks have experienced four tectonic settings (Fig. 13): continental rifting and sea-floor spreading, lithospheric subduction, continental collision, and

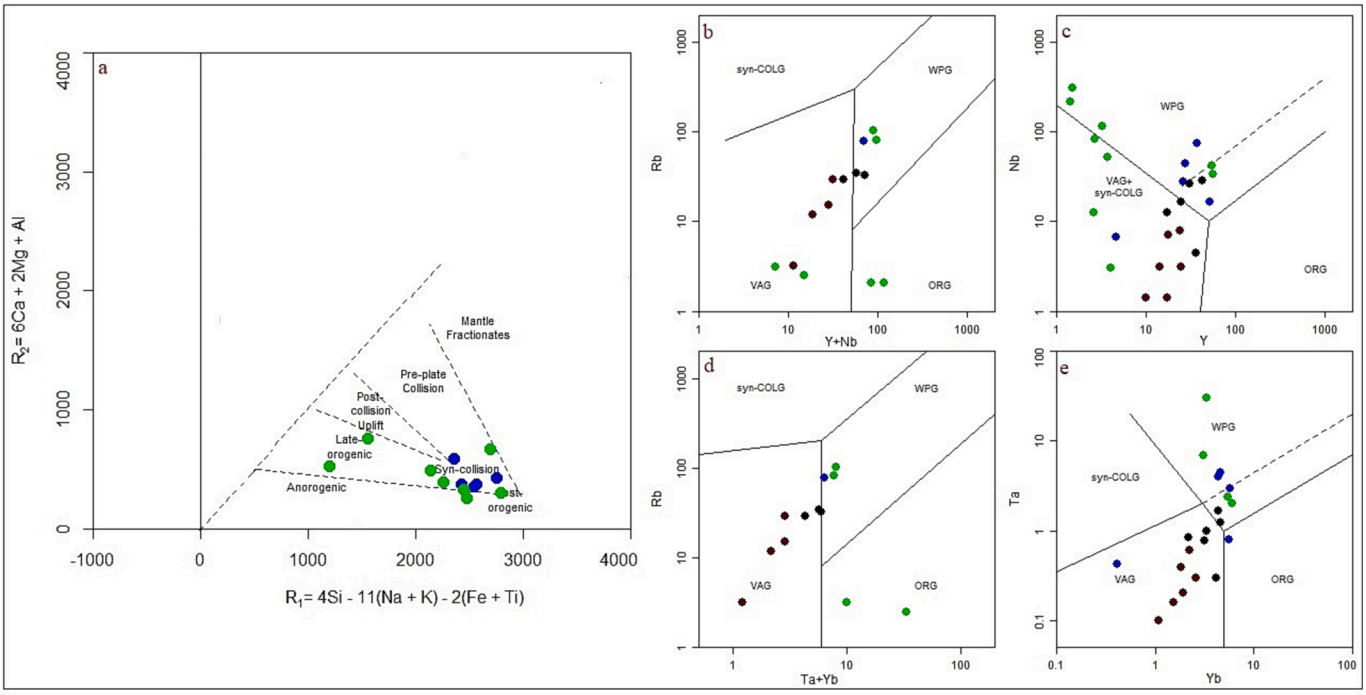

Fig. 12. Plot of R_1 vs. R_2 (after Batchelor and Bowden, 1985); Rb vs. Y + Nb & Ta + Yb, Ta vs. Yb, Nb vs. Y (after Pearce et al., 1984), for the granitoids of Gimbi-Nejo, west Ethiopian plateau. The symbols are the same as in Fig. 7.

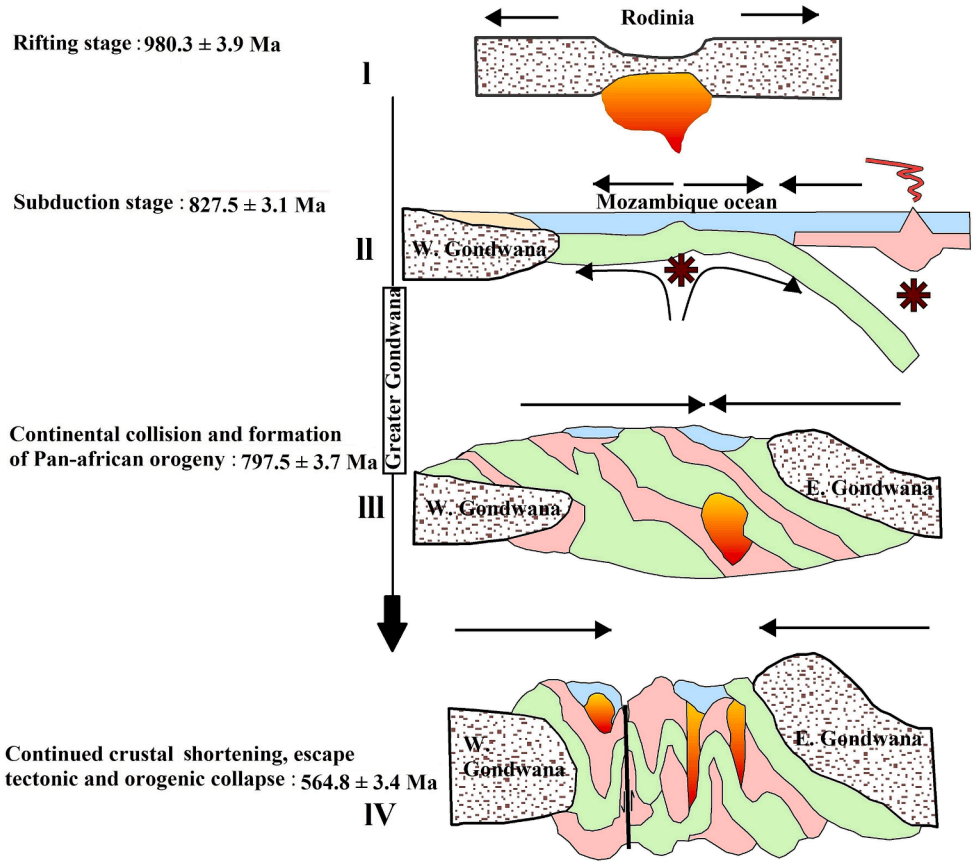

Fig. 13. The conceptual tectonic model for showing tectonic setting of Neoproterozoic era.

crustal shortening during the Neoproterozoic era (980–564 Ma). The magma generated during this era is from a depleted mantle source. Further studies are strongly recommended in the vicinity of Gimbi-Nejo area to enhance the level of geological research in western Ethiopia.

6. Conclusion

The field mapping and geochemical study of intrusive and *meta*-intrusive rocks of the Pan-African basement of Gimbi-Nejo area, west Ethiopia yield the following conclusions:

1. The ice rafting deposits were first discovered in the west Ethiopian plateau, indicating the Neoproterozoic ice age.
2. Pan-African basement has experienced four tectonic stages during the Neoproterozoic era: continental rifting at ca. 980 Ma, lithospheric subduction at 827 Ma, continental collision at 797 Ma, and strike-slippage/crustal shortening at 564 Ma.
3. The in-situ Hf isotopic compositions of zircon grains suggest that Neoproterozoic granitoid magma originated from the partial melting of juvenile crust, which formed during the Meso-Neoproterozoic era at different time periods: 915–1233 Ma, 1217–860 Ma, 1181–698 Ma, and 1043–460 Ma. Some zircon grains from alkali-calcic granitoid suggest that the juvenile crust during the Neoproterozoic era was likely heterogeneous (εHf (t) = +7.11 to +17.1).
4. Neoproterozoic tholeiitic meta-peridotites and meta-gabbros to gabbros originated from partial melting of garnet-spinel lherzolite to spinel lherzolite (<10 %) and garnet lherzolite to garnet-spinel lherzolite (<30 %) mantle source, respectively.
5. The representative meta-granitoids are medium-K calc-alkaline peraluminous to metaluminous A-type granitoids while calc-granitoids are low to medium-K tholeiite peraluminous I-type granitoids, calc-alkalic granitoids are high-K calc-alkaline peraluminous I-type granitoids, and alkali-calcic granitoids are low to high-K calc-alkaline peraluminous-metaluminous I-S type granitoids.

Declaration of competing interest

The authors declare that they have no known competing financial interests or personal relationships that could have appeared to influence the work reported in this paper.

Data availability

Data will be made available on request.

Acknowledgments

We thank all project members from Wuhan center of China Geological Survey, Geophysical Exploration Brigade of Hubei Geological Bureau, and the collaborators from Geological Survey of Ethiopia. Special thanks to the Embassy of the People's Republic of China in Ethiopia for their support during work, and to Editor-in-chief Huayong Chen and the anonymous reviewers for critical comments and constructive suggestions, which improved the quality of the paper. We also acknowledge the laboratory's analytical support.

Funding

This work was supported by the National Natural Science Foundation of China (No. 92055212), China Commerce Ministry (foreign-aid project (2007)420) and the Ministry of science and technology, China (International cooperation project no. 2009DFA20630).

Appendix A. Supplementary data

Supplementary data to this article can be found online at https://doi.org/10.1016/j.oregeorev.2023.105858.

References

Abbate, E., Bruni, P., Sagri, M., 2015. Geology of Ethiopia: a review and geomorphological perspectives. Landscapes Landforms Ethiopia 33–64.

Abdelsalam, M.G., Stern, R.J., 1996. Sutures and shear zones in the Arabian-Nubian Shield. J. Afr. Earth Sci. 23 (3), 289–310.

Abraham, A., 1989. Tectonic history of the Pan-African low-grade belt of western Ethiopia. Ethiopian Institute of Geological Survey, Addis Ababa, p. 22.

Agrawal, S., Guevara, M., Verma, S., 2008. Tectonic discrimination of basic and ultrabasic volcanic rocks through log-transformed ratios of immobile trace elements. Int. Geol. Rev. 50, 1057–1079.

Aldanmaz, E., Pearce, J.A., Thirlwall, M., et al., 2000. Petrogenetic evolution of late Cenozoic, post-collision volcanism in western Anatolia, Turkey. J. Volcanol. Geoth. Res. 102 (1–2), 67–95.

Tadesse Alemu, Tsegaye Abebe, 2000. Geology of the Gimbi area, compiled by Geological Survey of Ethiopia,158p.

Ali, K.A., Zoheir, B.A., Stern, R.J., Andresen, A., Whitehouse, M.J., Bishara, W.W., 2016. Lu-Hf and O isotopic compositions on single zircons from the North Eastern Desert of Egypt, Arabian-Nubian Shield: implications for crustal evolution. Gondwana Res. 32, 181–192.

Allen, A., Tadesse, G., 2003. Geological setting and tectonic subdivision of the Neoproterozoic orogenic belt of Tuludimtu, western Ethiopia. J. Afr. Earth Sci. 36 (4), 329–343.

Alves, A., Janasi, V.A., Campos Neto, M.C., Heaman, L., Simonetti, A., 2013. U-Pb geochronology of the granite magmatism in the Embu Terrane: implications for the evolution of the Central Ribeira Belt, SE Brazil. Precambr. Res. 230, 1–12.

Amam, A.G., 2001. Petrology and geochemistry of granite and syenite from Perhentian Island, Peninsular Malaysia. Geosci. J. 5 (2), 123.

Andersen, T., Kristoffersen, M., Elburg, M.A., 2016. How far can we trust provenance and crustal evolution information from detrital zircons? A South African case study. Gondwana Res. 34, 129–148.

Antoine, T., Antoine, T., Julien, B., Jean-Marc, B., Hervé, D., Nasser, E., Gaëlle, P., Christophe, M., Arnaud, W., Olivier, B., Paul, S., Sara, V., 2015. The Tachakoucht-Iriri-Tourtit arc complex (Moroccan Anti-Atlas): Neoproterozoic records of polyphased subduction-accretion dynamics during the Pan-African orogeny. J. Geodyn. 96, 81–103. https://doi.org/10.1016/J.JOG.2015.07.004.

Asrat, A., Barbey, P., Gleizes, G., 2001. The Precambrian geology of Ethiopia: a review. Afr. Geosci. Rev. 8 (3/4), 271–288.

Axelsson, E., Mezger, K., Ewing, T., 2020. The Kuunga Orogeny in the Eastern Ghats Belt: Evidence from geochronology of biotite, amphibole and rutile, and implications for the assembly of Gondwana. Precambr. Res. 347, 105805.

Azevedo Sobrinho, J.M., Janasi, V.A., Simonetti, A., Heaman, L.M., Santoro, J., Diniz, H. N., 2011. The IlhaAnchieta Quartz Monzonite:the southernmost expression of ca, 500 Ma post-collisional magmatism in the Ribeira Belt. An. Acad. Bras. Ciênc. 83 (3), 891–906.

Baldo, E., Casquet, C., Pankhurst, R.J., Galindo, C., Rapela, C.W., Fanning, C.M., Dahlquist, J., Murra, J., 2006. Neoproterozoic A-Type Magmatism in the Western Sierras Pampeanas (argentina): Evidence for Rodinia Break-up along a Proto-Iapetus Rift?. 18 (6), 388–394. https://doi.org/10.1111/j.1365-3121.2006.00703.x.

Barbarin, B., 1999. A review of the relationships between granitoid types, their origins and their geodynamic environments. Lithos 46 (3), 605–626.

Bas, M.L., Maitre, R.L., Streckeisen, A., et al., 1986. A chemical classification of volcanic rocks based on the total alkali-silica diagram. J. Petrol. 27 (3), 745–750.

Basei, M.A.S., Frimmel, H.E., Nutman,A.P., Preciozzi, F., 2008a.West Gondwana amalgamation based on detrital zircon ages from Neoproterozoic Ribeira and Dom Feliciano belts of South America and comparison with coeval sequences from SW Africa. In: Pankhurst, R.J., Trouw, R.A.J., Brito Neves, B.B., de Wit, M.J. (Eds.), West Gondwana: Pre-Cenozoic Correlations Across the South Atlantic Region, vol. 294. Geological Society London, London, pp. 239–256, Special Publication.

Batchelor, R.A., Bowden, P., 1985. Petrogenetic interpretation of granitoid rock series using multicationic parameters. Chem. Geol. 48 (1–4), 43–55.

Batumike, J.M., O'Reilly, S.Y., Griffin, W.L., Belousova, E.A., 2007. U-Pb and Hf-isotope analyses of zircon from the Kundelungu Kimberlites, D.R. Congo: Implications for crustal evolution. Precambr. Res. 156, 195–225.

Bauernhofer, A., Christoph, H., Wallbrecher, E., Muhongo, S., Hoinkes, Georg, Mogessie, Aberra, Opiyo-Akech, Norbert, Tenczer, V., 2009. Geochemistry of basement rocks from SE Kenya and NE Tanzania: indications for rifting and early Pan-African subduction. Int. J. Earth Sci. 98 (8), 1809–1834. https://doi.org/10.1007/S00531-008-0345-9.

Be'eri-Shlevin, Y., Katzir, Y., Whitehouse, M.J., Kleinhanns, C.I., 2009. Contribution of pre-Pan-African crust to formation of the Arabian Nubian Shield: New secondary ionization mass spectrometry U-Pb and O studies of zircon. Geology 37, 899–902.

Bento dos Santos, T., Munhá, J., Tassinari, C., Fonseca, P., Dias Neto, C., 2010. Thermochronology of central Ribeira Fold Belt, SE Brazil: petrological and geochronological evidence for high-temperature maintenance during Western Gondwana amalgamation. Precambr. Res. 180 (3–4), 285–298.

Beyth, M., Avigad, D., Wetzel, H.-U., et al., 2003. Crustal exhumation and indications for Snowball Earth in the East African Orogen: north Ethiopia and east Eritrea. Precambr. Res. 123 (2–4), 187–201.

Borba, A.W., Mizusaki, A.M.P., Santos, J.O.S., McNaughton, N.J., Onoe, A.T., Hartmann, L.A., 2008. U-Pb zircon and 40Ar–39Ar K-feldspar dating of synsedimentary volcanism ofthe Neoproterozoic Maricá Formation: constraining the age of foreland basin inception and inversion in the Camaquã Basin of southern Brazil. Basin Res. 20, 359–375.

Bowden, S., Gani, N.D., Alemu, T., O'Sullivan, P., Abebe, B., Tadesse, K., 2019. Evolution of the Western Ethiopian Shield revealed through U-Pb geochronology, petrogenesis, and geochemistry of syn- and post-tectonic intrusive rocks. Precambr. Res. https://doi.org/10.1016/j.precamres.2019.105588.

Boyton, W., 1984. Geochemistry of the rare earth elements: meteorite studies. Rare earth element geochemistry. Elsevier, Amsterdam, pp. 63–114.

Cai, Y., Ni, P., Wang, G., Chen, H., 2023. Geochemical Characteristics of the Granodiorite Porphyry in Dongxiang W-Cu Deposit, SE China. Minerals, 13, 380. https:// doi.org/10.3390/min13030380.

Cawood, P.A., Buchan, C., 2007. Linking accretionary orogenesis with supercontinent assembly. Earth Sci. Rev. 82 (3–4), 217–256. https://doi.org/10.1016/j.earscirev.2007.02.002.

Chemale Jr., F., Mallmann, G., Bitencourt, M.F., Kawashita, K., 2012. Time constraints on magmatism along the Major Gercino Shear Zone, Southern Brazil: implications for West Gondwana reconstruction. Gondwana Res. 22 (1), 184–199.

Christopher, S., Carl, W., Hoiland, Ron, Harris, Paul, Link, K., Balgord, Elizabeth, 2012. Constraining the timing and provenance of the Neoproterozoic Little Willow and Big Cottonwood Formations, Utah: Expanding the sedimentary record for early rifting of Rodinia. Precambr. Res. 204, 57–65. https://doi.org/10.1016/J.PRECAMRES.2012.02.009.

Coleman, R.G., 1980. Handbook of chemical analysis of rocks. John Wiley & Sons.

Collins, A., Blades, M., Cox, G., Alessio, B., Foden, J., Merdith, A., Müller, D., 2018. Neoproterozoic Arabia-The Angudan/Malagasy orogenic collision of Neoproterozoic India with Africa in a plate kinematic framework. In: EGU General Assembly Conference Abstracts, p. 2710.

Condie, K.C., 2005. TTGs and Adakites: Are They Both Slab Melts? Lithos 80, 33–44. https://doi.org/10.1016/j.lithos.2003.11.001.

Daniel, T., Brennan, Daniel, Brennan, T., David, M., Pearson, Paul, Link, K., Kevin, R., Chamberlain, R., 2020. Neoproterozoic Windermere Supergroup Near Bayhorse, Idaho: Late-Stage Rodinian Rifting Was Deflected West Around the Belt Basin. Tectonics 39 (8). https://doi.org/10.1029/2020TC006145.

David, Evans, 2021. Meso-Neoproterozoic Rodinia Supercycle. 549-576. doi: 10.1016/B978-0-12-818533-9.00006-0.

David, C., Greene, 2010. Neoproterozoic rifting in the southern Georgina Basin, central Australia: Implications for reconstructing Australia in Rodinia. Tectonics 29 (5). https://doi.org/10.1029/2009TC002543.

DePaolo, D.J., 1981. Trace element and isotopic effects of combined wallrock assimilation and fractional crystallization. Earth Planet. Sci. Lett. 53 (2), 189–202.

Dey, A., Hussain, M.F., Barman, M.N., 2018. Geochemical characteristics of mafic and ultramafic rocks from the Naga Hills Ophiolite, India: implications for petrogenesis. Geosci. Front. 9 (2), 517–529.

Eby, G.N., 1992. Chemical subdivision of the A-type granitoids: petrogenetic and tectonic implications. Geology 20 (7), 641–644.

Elhlou, S., Belousova, E., Griffin, W. L., et al., 2006. Trace element and isotopic composition of GJ-red zircon standard by laser ablation. Geochim. Cosmochim. Acta, 70(18), 158.

Elizabeth, McClellan, Esteban, G., 2014. The Cryogenian intra-continental rifting of Rodinia: Evidence from the Laurentian margin in eastern North America. Lithos 206, 321–337. https://doi.org/10.1016/J.LITHOS.2014.08.006.

Elizabeth, B., Yonkee, W., Paul, A., Link, K., Christopher, Fanning, 2013. Stratigraphic, geochronologic, and geochemical record of the Cryogenian Perry Canyon Formation, northern Utah: Implications for Rodinia rifting and snowball Earth glaciation. Geol. Soc. Am. Bull. 125, 1442–1467. https://doi.org/10.1130/B30860.1.

Ferraccioli, F., Jones, P.C., Curtis, M.L., Leat, P.T., Jordan, T.A., Corr, H.F., Ritzwoller, M. H., 2011. East Antarctic rifting triggers uplift of the Gamburtsev Mountains. Nature 479 (7373), 388–392.

Ghebretensae Ghebsha Fitwi, Yao, Hua-Zhou, Zhao Kai, Zhao Jun-Hong, 2019. Petrogenesis and tectonic implications of the Neoproterozoic adakitic and A-type granitoids in the southern Arabian-Nubian shield. Arab. J. Geosci., 12(14), 428. doi: 10.1007/s12517-019-4575-x.

Frimmel, H.E., Basei, M.A.S., Correa, V.X., Mbangula, N., 2013. A new lithostratigraphic subdivision and geodynamic model for the Pan-African western Saldania Belt, South Africa. Precambr. Res. 231, 218–235.

Frost, B.R., Barnes, C.G., Collins, W.J., et al., 2001. A geochemical classification for granitic rocks. J. Petrol. 42 (11), 2033–2048.

Ganade de Araujo, C.E., Rubatto, D., Hermnn, J., Cordani, U.G., Caby, R., Basei, M.A.S., 2014. Ediacaran 2500 km long synchronous deep continental subduction in the west Gondwana orogen. Nat. Com. 5.

Gradim, C., Roncato, J., Pedrosa-Soares, A.C., Cordani, U.G., Dussin, I., Alkmim, F.F., Queiroga, G., Jacobsohn, T., Silva, L.C., Babinski, M., 2014. The hot back-arc zone of the Araçuaí orogen, Eastern Brazil: from sedimentation to granite generation. Braz. J. Geol. 44 (1), 155–180.

Gradstein, F.M., Ogg, J.G., Schmitz, M.D., Ogg, G.M., 2018. The Geologic Time Scale 2018. Elsevier.

Grenne, T., Pedersen, R.B., Bjerkgård, T., Braathen, A., Selassie, M.G., Worku, T., 2003. Neoproterozoic evolution of Western Ethiopia: igneous geochemistry, isotope systematics and U-Pb ages. Geol. Mag. 140, 373–395.

Griffin, W., Graham, S., O'Reilly, S.Y., et al., 2004. Lithosphere evolution beneath the Kaapvaal Craton: Re–Os systematics of sulfides in mantle-derived peridotites. Chem. Geol. 208 (1–4), 89–118.

Hackspacher, P., Dantas, E.L., Spoladore, A., Fetter, A.H., Oliveira, M.A.F., 2000. Evidence of Neoproterozoic backarc basin development in the Central Ribeira Belt, Southeastern Brazil: new geochronological and geochemical constrains from the São Roque – Ac¸ungui Groups. Rev. Bras. Geociênc. 30 (1), 110–114.
Hanson, R.E., Wilson, T.J., Munyanyiwa, H., 1994. Geologic evolution of the Neoproterozoic Zambezi orogenic belt in Zambia. J. Afr. Earth Sc. 18 (2), 135–150.
Hardarson, B.S., 2015. The western branch of the East African Rift: A review of tectonics, volcanology and geothermal activity. GRC Trans. 39, 239–246.
Hartmann, L.A., Santos, J.O., Bossi, J., Campal, N., Schiplov, A., McNaughton, N., 2002. Zircon and titanite U-Pb SHRIMP geochronology of Neoproterozoic felsic magmatism on the eastern border of the Rio de La Plata Craton, Uruguay. J. S. Am. Earth Sci. 15, 229–236.
Hoffman, P.F., 1991. Did the breakout of Laurentia turn Gondwanaland inside-out? Science 252 (5003), 1409–1412.
Hoffman, P.F., Abbot, D.S., Ashkenazy, Y., Benn, D.I., Brocks, J.J., Cohen, P.A., Young, E. D., 2017. Snowball Earth climate dynamics and Cryogenian geology-geobiology. Sci. Adv. 3 (11), e1600983.
Hu, Z., Liu, Y., Gao, S., et al., 2012. Improved in situ Hf isotope ratio analysis of zircon using newly designed X skimmer cone and jet sample cone in combination with the addition of nitrogen by laser ablation multiple collector ICP-MS. J. Anal. At. Spectrom 27 (9), 1391–1399.
Irvine, T.N., Baragar, W., 1971. A guide to the chemical classification of the common volcanic rocks. Can. J. Earth Sci. 8 (5), 523–548.
Jam, M.Q., Agheem, M.H., Khan, T., Rehman, H.U., Markhand, A.H., 2022. Geochemistry and Petrogenesis of the Wadhrai Granite Stock of the Malani Igneous Suite in Nagar Parkar Area, SE Pakistan. Minerals 12 (10), 1240.
Jenner, G., Foley, S., Jackson, S., et al., 1993. Determination of partition coefficients for trace elements in high pressure-temperature experimental run products by laser ablation microprobe-inductively coupled plasma-mass spectrometry (LAM-ICP-MS). Geochim. Cosmochim. Acta 57 (23–24), 5099–5103.
Jensen, L., 1976. A new cation plot for classifying subalkalic volcanic rocks. Misc. Pap 66, 22.
Jiawei, Z., Taiping, Y.e., Yaran, D., Jianshu, C., Hui, Z., Chuangu, D., Guohua, Y., Kaiyuan, J., 2019. Provenance and tectonic setting transition as recorded in the Neoproterozoic strata, western Jiangnan Orogen: Implications for South China within Rodinia. Geosci. Front. 10 (5), 1823–1839. https://doi.org/10.1016/J.GSF.2018.10.009.
Jiří, K., Vojtěch, J., Pedro, O., Jiří, S., Stanislav, U., 2017. Did the circum-Rodinia subduction trigger the Neoproterozoic rifting along the Congo-Kalahari Craton margin? Int. J. Earth Sci. 107 (5), 1859–1894. https://doi.org/10.1007/S00531-017-1576-4.
Johnson, P., Abdelsalam, M., Stern, R., 2002. The Bi'r Umq-Nakasib Shear zone: geology and structure of a Neoproterozoic suture in the northern East African Orogen, Saudi Arabia and Sudan. Saudi Geol. Survey Techn. Rep. SGS-TR-2002-1, 33.
Johnson, P.R., Andresen, A., Collins, A.S., Fowler, A.R., Fritz, H., Ghebreab, W., Kusky, T., Stern, R.J., 2011. Late Cryogenian-Ediacaran history of the Arabian-Nubian shield: a review of depositional, plutonic, structural, and tectonic events in the closing stages of the northern East African Orogen. J. Afr. Earth Sci. 61, 167–232.
Johnson, T.E., Ayalew, T., Mogessie, A., Kruger, F.J., Poujol, M., 2004. Constraints on the tectonometamorphic evolution of the Western Ethiopia Shield. Precambr. Res. 133, 305–327.
Joy, S., Linde, G., Choudhury, A., Deb, G., Tappe, S., 2018. Reassembly of the Dharwar and Bastar cratons at ca. 1 Ga: Evidence from multiple tectonothermal events along the Karimnagar granulite belt and Khammam schist belt, southern India. J. Earth Syst. Sci.
Junaid, K., Yao, H.-Z., Chen, K.-X., et al., 2022. Geochemical prospecting of polymetallic mineralization in Gimbi-Nejo area, West Ethiopia. Ore Geol. Rev. 105117.
Karlstrom, Karl E.; Bowring, Samuel A.; Dehler, Carol M.; Knoll, Andrew H.; Porter, Susannah M.; Des Marais, David J.; Weil, Arlo B.; Sharp, Zachary D.; Geissman, John W.; Elrick, Maya B.; Timmons, J. Michael; Crossey, Laura J.; Davidek, Kathleen L., 2000. Chuar Group of the Grand Canyon: Record of breakup of Rodinia, associated change in the global carbon cycle, and ecosystem expansion by 740 Ma. Geology, 28 (7), 619–. doi:10.1130/0091-7613(2000)28<619:CGOTGC>2.0.CO;2.
Kazmin, V., 1971. Precambrian of Ethiopia. Nat. Phys. Sci., Lond. 230 (16), 176–177.
Kazmin, V., 1973. Geological map of Ethiopia (scale 1: 2,000,000). Geological Survey of Ethiopia, Addis Ababa.
Kazmin, V., 1975. The Precambrian of Ethiopia and some aspects of the geology of the Mozambique Belt. Geophys. Observ. Bull. 1 (15), 27–43.
Kazmin, V., Shifferaw, A., Balcha, T., 1978. The Ethiopian basement: stratigraphy and possible manner of evolution. Geol. Rundsch. 67 (2), 531–546.
Kebede, T., Kloetzli, U., Koeberl, C., 2000. Single-grain zircon $^{207}Pb/^{206}Pb$ ages and evolution of granitoid magmatism in western Ethiopia. J. Afr. Earth Sci., 30(4), 45–45.
Kebede, T., Koeberl, C., Koller, F., 1999. Geology, geochemistry and petrogenesis of intrusive rocks of the Wallagga area, western Ethiopia. J. Afr. Earth Sc. 29 (4), 715–734.
Kebede, T., Kloetzli, U.S., Koeberl, C., 2001. U/Pb and Pb/Pb zircon ages from granitoid rocks of Wallagga area: constraints on magmatic and tectonic evolution of Precambrian rocks of Western Ethiopia. Mineral Petrol 71, 251–271.
Kebede, T., Horie, K., Hidaka, H., Terada, K., 2007. Zircon 'microvein' in peralkaline granitic gneiss, Western Ethiopia: origin, SHRIMP U-Pb geochronology and trace element investigations. Chem. Geol. 242, 76–102.
Kee, W.-S., Won, K.S., Sanghoon, K., Santosh, M., Kyoungtae, K.o., Youn-Joong, J., 2019. Early Neoproterozoic (ca. 913–895 Ma) arc magmatism along the central–western Korean Peninsula: Implications for the amalgamation of Rodinia supercontinent. Precambr. Res. 335 https://doi.org/10.1016/j.precamres.2019.105498.
Khan, J., Yao, H., Zhao, J., Li, Q., Xiang, W., Jiang, J., Tahir, A., 2023. Petrogenesis and Tectonic Implications of the Tertiary Choke Shield Basalt and Continental Flood Basalt from the Central Ethiopian Plateau. J. Earth Sci. 34 (1), 86–100.
Kraus, S., 2005. Magmatic dyke systems of the South Shetland Islands volcanic arc (West Antarctica): reflections of the geodynamic history. Als Dissertation 1–160.
Kristoffersen, M., Andersen, T., Elburg, M.A., Watkeys, M.K., 2016. Detrital zircon in a supercontinental setting: locally derived and far-transported components in the Ordovician Natal Group, South Africa. J. Geol. Soc. London 173, 203–215. https://doi.org/10.1144/jgs2015-012.
Kröner, A.S.R.J., 2004. Pan-African Orogeny. Encycl. Geol. 1, 1–12.
Kröner, A., Stern, R., Dawoud, A.S., et al., 1987. The Pan-African continental margin in northeastern Africa: evidence from a geochronological study of granulites at Sabaloka, Sudan. Earth Planet. Sci. Lett. 85 (1–3), 91–104.
Kwékam, M., Affaton, P., Bruguier, O., Liégeois, J.-P., Hartmann, G., Njonfang, E., 2013. The Pan-African Kekam gabbro-norite (West-Cameroon), U-Pb zircon age, geochemistry and Sr-Nd isotopes: Geodynamic implication for the evolution of the Central Africa fold belt. J. Afr. Earth Sci. 84, 70–88.
Li, Z.X., Evans, D.A.D., Zhang, S., 2019. The paleogeography of late Neoproterozoic and Early Cambrian time: Evidence from integrated paleomagnetism and geochronology. Gondw. Res. 67, 56–83.
Li, Xian-hua, 2001. Zircon U-Pb age and petrochemical characteristics of the Neoproterozoic bimodal volcanics from western Yangtze block.
Liangshu, S., Deng, X.L., Wenbin, Zhu, Dongsheng, Ma, Wenjiao, Xiao, 2011. Precambrian tectonic evolution of the Tarim Block, NW China: New geochronological insights from the Quruqtagh domain. J. Asian Earth Sci. 42 (5), 774–790. https://doi.org/10.1016/J.JSEAES.2010.08.018.
Lissan, N.H., Bakheit, A.K., 2011. Geochemistry and Geotectonic Setting of Neoproterozoic Granitoids from Artoli Area, Berber Province, Northern Sudan. J. Appl. Sci. 11 (5), 752–767.
Liu, Y., Gao, S., Hu, Z., et al., 2010. Continental and oceanic crust recycling-induced melt–peridotite interactions in the Trans-North China Orogen: U-Pb dating, Hf isotopes and trace elements in zircons from mantle xenoliths. J. Petrol. 51 (1–2), 537–571.
Ludwig, K., 2003. User's manual for Isoplot 3.00: A geochronological toolkit for Microsoft Excel. Spec. Publ. 4a.
Maas, R., Kinny, P.D., Williams, I.S., et al., 1992. The Earth's oldest known crust: a geochronological and geochemical study of 3900–4200 Ma old detrital zircons from Mt. Narryer and Jack Hills, Western Australia. Geochim. Cosmochim. Acta 56 (3), 1281–1300.
Manda, B.W.C., Cawood, P.A., Spencer, C.J., Prave, T., Robinson, R., Roberts, N.M.W., 2019. Evolution of the Mozambique Belt in Malawi constrained by granitoid U-Pb, Sm-Nd and Lu- Hf isotopic data. Gondwana Res. 68, 93–107.
Manikyamba, C., Ganguly, S., Pahari, A., 2021. Geochemical Features of Bellara Trap Volcanic Rocks of Chitradurga Greenstone Belt, Western Dharwar Craton, India: Insights into MORB-BABB Association from a Neoarchean Back-Arc Basin. J. Earth Sci. 32 (6), 1528–1544. https://doi.org/10.1007/s12583-021-1472-5.
McKenzie, D., O'nions, R., 1991. Partial melt distributions from inversion of rare earth element concentrations. J. Petrol. 32 (5), 1021–1091.
Moller, A., Mezger, K., Schenk, V., 2000. U-Pb dating of metamorphic minerals: PanAfrican metamorphism and prolonged slow cooling of high pressure granulites in Tanzania, East Africa. Precambr. Res. 104, 123–145.
Morag, N., Avigad, D., Gerdes, A., Belousova, E., Harlavan, Y., 2011. Crustal evolution and recycling in the northern Arabian-Nubian Shield: new perspectives from zircon Lu-Hf and U Pb systematics. Precambr. Res. 186, 101–116.
Mosley, P., 1993. Geological evolution of the late Proterozoic "Mozambique Belt" of Kenya. Tectonophysics 221 (2), 223–250.
Noce, C., Pedrosa-Soares, A.C., Silva, L., Armstrong, R., Piuzana, D., 2007. Evolution of polycyclic basement complexes in the Arac¸uaí Orogen based on U-Pb SHRIMP data: implications for Brazil-Africa links in Paleoproterozoic time. Precambr. Res. 159 (1–2), 60–78.
Novo, T.A., Pedrosa-Soares, A.C., Noce, C.M., Alkmim, F.F., Dussin, I., 2010. Rochas charnockíticas do sudeste de Minas Gerais: a raiz granulítica do arco magmático do Orógeno Arac¸uaí. Rev. Bras. Geociênc. 40, 573–592.
O'Conner, J., 1965. A classification of quartz-rich igneous rocks based on feldspar ratios. US Geol. Surv. Prof, Paper, p. 82.
Otamendi, J.E., Ducea, M.N., Tibaldi, A.M., et al., 2009. Generation of tonalitic and dioritic magmas by coupled partial melting of gabbroic and metasedimentary rocks within the deep crust of the Famatinian magmatic arc, Argentina. J. Petrol. 50 (5), 841–873.
Paulsson, O., andreasson, P.G., 2002. Attempted break-up of Rodinia at 850 Ma: geochronological evidence from the Seve-Kalak Superterrane, Scandinavian Caledonides. J. Geol. Soc. Lond. 159 (6), 751–761. https://doi.org/10.1144/0016-764901-156.
Pearce, J.A., Harris, N.B., Tindle, A.G., 1984. Trace element discrimination diagrams for the tectonic interpretation of granitic rocks. J. Petrol. 25 (4), 956–983.
Peccerillo, A., Taylor, S., 1976. Geochemistry of Eocene calc-alkaline volcanic rocks from the Kastamonu area, northern Turkey. Contrib. Mineral. Petrol. 58 (1), 63–81.
Pedrosa-Soares, A.C., de Campos, C.P., Noce, C., Silva, L.C., Novo, T., Roncato, J., Medeiros, S., Castaneda, C., Queiroga, G., Dantas, E., Dussini, I., Alkmim, F., 2011. Late Neoproterozoic–Cambrian granitic magmatism in the Arac¸uaí orogen (Brazil), the Eastern Brazilian Pegmatite Province and related mineral resources. In: Sial, A. N., Bettencourt, J.S., De Campos, C.P., Ferreira, V.P. (Eds.), Granite-Related Ore Deposits, vol. 350. Geo. Soc. Lon., pp. 25–51, Special Publications.
Petitgirard, S., Vauchez, A., Egydio-Silva, M., Bruguier, O., Camps, P., Monié, P., Babinski, M., Mondou, M., 2009. Conflicting structural and geochronological data

from the Ibituruna quartz-syenite (SE Brazil): effect of protracted "hot" orogeny and slow cooling rate? Tectonophysics 477, 174–196.
Piotr, K., Poprawa, P., Mateusz, Mikołajczak, Stanisław, Mazur, Michal, Malinowski, 2018. Deeply concealed half-graben at the SW margin of the East European Craton (SE Poland)-Evidence for Neoproterozoic rifting prior to the break-up of Rodinia. J. Palaeogeogr. 7 (1), 88–97. https://doi.org/10.1016/J.JOP.2017.11.003.
Polat, A., Hofmann, A.W., Rosing, M.T., 2002. Boninite-like volcanic rocks in the 3.7–3.8 Ga Isua greenstone belt, West Greenland: geochemical evidence for intra-oceanic subduction zone processes in the early Earth. Chem. Geol. 184, 231–254.
Polat, A., Hofmann, A.W., 2003. Alteration and geochemical patterns in the 3.7–3.8 Ga Isua greenstone belt, West Greenland. Precambr. Res. 126 (3–4), 197–218.
Prazeres Filho, H.J., Unpublished PhD thesis, 2005. Caracterizac¸ ão geológica e petrogenética do Batólito Granítico Três Córregos (PR-SP): Geoquímica Isotópica (Nd–Sr–Pb, Idades IDTIMS/SHRIMP e O18 em zircão). University of São Paulo, pp. 207.
Rahman, E. M. A., 1993. Geochemical and geotectonic controls of the metallogenic evolution of selected ophiolite complexes from the Sudan (Vol. 145). Fachbereich Geowiss, FU Berlin.
Richards, J.P., Kerrich, R., 2007. Special paper: adakite-like rocks: their diverse origins and questionable role in metallogenesis. Econ. Geol. 102 (4), 537–576.
Rino, S., Kon, Y., Sato, W., et al., 2008. The Grenvillian and Pan-African orogens: world's largest orogenies through geologic time, and their implications on the origin of superplume. Gondw. Res. 14 (1–2), 51–72.
Rollinson, H.R., 1993. Using geochemical data: Evaluation, presentation, interpretation. Longman Scientific and Technical, Wiley, New York, p. 352.
Ruibao, L.i., Xianzhi, P., Shuanhai, Y., Liyong, W., Zuochen, L.i., Gaoxue, Y., Duoxun, X. u., Mannian, L., Ting, K., 2016. Mid-Neoproterozoic Tadong amphibolites at the junction of the East Kunlun and Western Qinling Orogens – a record of continental rifting during the break-up of Rodinia. Int. Geol. Rev. 58 (4), 455–470. https://doi.org/10.1080/00206814.2015.1089423.
Samson, S.D., Inglis, J.D., D'Lemos, R.S., Admou, H., Blichert-Toft, J., Hefferan, K., 2004. Geochronological, geochemical, and Nd–Hf isotopic constraints on the origin of Neoproterozoic plagiogranites in the Tasriwine ophiolite, Anti-Atlas orogeny, Morocco. Precambr. Res. 135 (1), 133–147.
Shellnutt, J.G., Dostal, J., Keppie, J.D., 2004. Petrogenesis of the 723 Ma Coronation sills. Amundsen Basin, Arctic Canada: Implications for the Break-up of Rodinia 129 (3–4). https://doi.org/10.1016/j.precamres.2003.10.006.
Shellnutt, J., Gregory, N., Ha, T., Pham, Steven, Denyszyn, W., Meng, Wan, Yeh, Tung, Yi, Lee, 2017. Timing of collisional and post-collisional Pan-African Orogeny silicic magmatism in south-central Chad. Precambr. Res. 301, 113–123. https://doi.org/10.1016/J.PRECAMRES.2017.08.021.
Siga Jr., O., Basei, M.A.S., Passarelli, C.R., Sato, K., Cury, L.F., Mcreath, I., 2009. Magmatic records of lower Neoproterozoic and upper Neoproterozoic in Itaiacoca Belt (Paraná- Brazil): zircon ages and lithostratigraphy studies. Gondwana Res. 197–208.
Silva, L.C., McNaughton, N.J., Hartmann, L.A., Fletcher, I.R., 2003. Zircon U-Pb SHRIMP dating of Serra dos Orgos and Rio de Janeiro gneissic granitic suites: implications for the (560 Ma) Brasiliano/Pan-Africancollage. Rev. Br as. Geociênc. 33 (2), 237–244.
Sláma, J., Košler, J., Condon, D.J., et al., 2008. Plešovice zircon-a new natural reference material for U-Pb and Hf isotopic microanalysis. Chem. Geol. 249 (1–2), 1–35.
Soltani, A., 2000. Geochemistry and geochronology of I-type granitoid rocks in the northeastern central Iran plate.
Song, J., Hanwen, Z., Yabin, H., Xiaofeng, L.i., Wang Xingyan, W.u., Li'ang, W.Z., 2022. Zircon U-Pb ages and Hf isotopic compostions of Sugensala pluton in the western Junggar: Constraints on the tectonic evolution[J]. Geol. China 49 (5), 1624–1635 in Chinese with English abstract.
Stéphane, G., Yao, A., Jérôme, B., Julien, B., Guillaume, D., Nadege, H., René-Pierre, M., Stéphane, S., 2018. Transition from subduction to collision recorded in the Pan-African arc complexes (Mali to Ghana). Precambr. Res. 320, 261–280. https://doi.org/10.1016/J.PRECAMRES.2018.11.007.
Stern, R.J., 1994. Arc-assembly and continental collision in the Neoproterozoic African orogen: implications for the consolidation of Gondwanaland. Annu. Rev. Earth Planet. Sci. 22, 319–351.
Stern, R., Avigad, D., Miller, N., et al., 2006. Evidence for the snowball Earth hypothesis in the Arabian-Nubian Shield and the East African Orogen. J. Afr. Earth Sc. 44 (1), 1–20.
Sun, S.-S., McDonough, W. F., 1989. Chemical and isotopic systematics of oceanic basalts: implications for mantle composition and processes. In: Saunders, A.D., Norry, M.J., Eds., Ž. Magmatism in the Ocean Basins. Geological Society, London, Special Publications, 42(1): 313-345.
Tadesse, T., 1996. Structure across a possible intra-oceanic suture zone in the low-grade Pan-African rocks of northern Ethiopia. J. Afr. Earth Sc. 23 (3), 375–381.
Tadesse, G., Allen, A., 2005. Geology and geochemistry of the Neoproterozoic Tuludimtu Ophiolite suite, western Ethiopia. J. Afr. Earth Sc. 41 (3), 192–211.
Tadesse, T., Hoshino, M., Suzuki, K., Iizumi, S., 2000. Sm–Nd, Rb–Sr and Th–U–Pb zircon ages of syn- to post-tectonic granitoids from the Axum area of northern Ethiopia. J Afr Earth Sci 30, 313–327. https://doi.org/10.1016/S0899-5362(00)00022-1.
Tadesse-Alemu, A., 1998. Geochemistry of Neoproterozoic granitoids from the Axum area, northern Ethiopia. J. Afr. Earth Sc. 27 (3–4), 437–460.
Tassinari, C.C.G., Babinski, M., Nutman, A.P., 2004. A Idade e Natureza da Fonte do Granito do Moinho, Faixa Ribeira, Sudeste do Estado de São Paulo. Rev. Inst. Geociênc. – USP 4 (1), 91–100.
Tatsumi, Y., Eggins, S., 1995. Subduction Zone Magmatism. Blackwell, Oxford, p. 211.
Taylor, S.R., McLennan, S.M., 1995. The geochemical evolution of the continental crust. Rev. Geophys. 33 (2), 241–265.
Telmo, B., dos Santos, Colombo, Celso, Gaeta, Tassinari, Paulo, Fonseca, E., 2015. Diachronic collision, slab break-off and long-term high thermal flux in the Brasiliano–Pan-African orogeny: Implications for the geodynamic evolution of the Mantiqueira Province. Precambr. Res. 260, 1–22. https://doi.org/10.1016/J.PRECAMRES.2014.12.018.
Thomas, R.J., Chevallier, L.P., Gresse, P.G., Harmer, R.E., Eglington, B.M., Armstrong, R. A., de Beer, C.H., Martini, J.E.J., de Kock, G.S., Macey, P.H., Ingram, B.A., 2002. Precambrian evolution of the Sirwa Window, Anti-Atlas orogen, Morocco. Precambr. Res. 118 (1), 1–57.
Tollo, R.P., Aleinikoff, J.N., Bordelon, D.C., Burton, W.C., Johnson, S.E., McLelland, J.M., Wang, H., 2004. Proterozoic tectonic evolution of the Grenville orogen in North America. GSA Today 14 (8), 4–11.
Vail, J.R., 1985. Pan-African (late Precambrian) tectonic terrains and the reconstruction of the Arabian-Nubian Shield. Geology 13 (12), 839–842.
Vervoort, J.D., Kemp, A.I.S., 2016. Clarifying the zircon Hf isotope record of crust–mantle evolution. Chem. Geol. 425, 65–75.
Wang, Jian, Li, Zheng-Xiang, 2003. History of Neoproterozoic Rift Basins in South China: Implications for Rodinia Break-up 122 (1–4). https://doi.org/10.1016/s0301-9268(02)00209-7.
Wang, X.-C., Li, X.-H., Li, W.-X., Li, Z.-X., Liu, Y., Yang, Y.-H., Liang, X.-R., Tu, X.-L., 2008. The Bikou basalts in the northwestern Yangtze block, South China: Remnants of 820–810 Ma continental flood basalts? Geol. Soc. Am. Bull. 120 (11–12), 1478–1492. https://doi.org/10.1130/B26310.1.
Wang, G.-D., Wang, H., Chen, H.-X., Zhang, B.o., Zhang, Q., Wu, C.-M., 2016. Geochronology and geochemistry of the TTG and potassic granite of the Taihua complex, Mts. Huashan: Implications for Crustal Evolution of the Southern North China Craton. Precambr. Res. https://doi.org/10.1016/j.precamres.2016.11.006.
Wang, F., Zheng, X.S., Lee, J.I., et al., 2009. An 40Ar/39Ar geochronology on a mid-Eocene igneous event on the Barton and Weaver peninsulas: Implications for the dynamic setting of the Antarctic Peninsula. Geochem. Geophys. Geosyst. 10 (12).
West, A.R., 2003. Igneous petrogenesis. Blackwell Publishing.
Williams, F.M., 2016. Understanding Ethiopia: Geology and Scenery. Springer International Publishing, GeoGuide.
Williams, I., Claesson, S., 1987. Isotopic evidence for the Precambrian provenance and Caledonian metamorphism of high grade parageneses from the Seve Nappes, Scandinavian Caledonides. Contrib. Mineral. Petrol. 97 (2), 205–217.
Woldemichael, B.W., Kimura, J.-I., 2008. Petrogenesis of the Bikilal Ghimbi gabbro, Western Ethiopia. J. Mineral Petrol. Sci. 103, 23–46.
Woldemichael, B.W., Kimura, J.-I., Dunkley, D.J., Tani, K., Ohira, H., 2009. SHRIMP U-Pb zircon geochronology and Sr–Nd isotopic systematic of the Neoproterozoic Ghimbi-Nedjo mafic to intermediate intrusions of Western Ethiopia: a record of passive margin magmatism at 855 Ma? Int. J. Earth Sci. (Geol. Rundsch.) 99, 1773–1790. https://doi.org/10.1007/s00531-009-0481-x.
Woldemichael, B.W., Kimura, J.-I., Dunkley, D.J., et al., 2010. SHRIMP U-Pb zircon geochronology and Sr–Nd isotopic systematic of the Neoproterozoic Ghimbi-Nedjo mafic to intermediate intrusions of Western Ethiopia: a record of passive margin magmatism at 855 Ma? Int. J. Earth Sci. 99 (8), 1773–1790.
Wood, D.A., 1980. The application of a Th–Hf–Ta diagram to problems of tectonomagmatic classification and to establishing the nature of crustal contamination of basaltic lavas of the British Tertiary volcanic province. Earth Planet. Sci. Lett. 50, 11–30.
Wu, Y.-B., 2005. Zircon U-Pb Age, Element and Oxygen Isotope Geochemisty of Neoproterozoic Granites at Shiershan in South Anhui Province. Geol. J. China Univ.
Wu, F.-Y., Yang, Y.-H., Xie, L.-W., et al., 2006. Hf isotopic compositions of the standard zircons and baddeleyites used in U-Pb geochronology. Chem. Geol. 234 (1–2), 105–126.
Xiaozhuang, C., Xiaozhuang, C., Xinsheng, J., Xinsheng, J., Jian, W., Jian, W., Xuan-Ce, W., JieWen, Z., JieWen, Z., Qi, D., Qi, D., Shiyong, L., Hao, W.u., Zhuo-Fei, J., Ya-Nan, W., 2015. Mid-Neoproterozoic diabase dykes from Xide in the western Yangtze Block, South China: New evidence for continental rifting related to the breakup of Rodinia supercontinent. Precambr. Res. 268 (268), 339–356. https://doi.org/10.1016/J.PRECAMRES.2015.07.017.
Xu, Xue-yi, 2009. Mid-Neoproterozoic Rift-related Volcanic Rocks in South China: Geological Records of Rifting and Break-up of the Supercontinent Rodinia. Northwestern Geology.
Yibas, B., Reimold, W., Armstrong, R., et al., 2002. The tectonostratigraphy, granitoid geochronology and geological evolution of the Precambrian of southern Ethiopia. J. Afr. Earth Sc. 34 (1–2), 57–84.
Yiming, L., Yuhua, W., Sanzhong, L.i., Santosh, M., Guo, Runhua, Shengyao, Yu, 2021. Neoproterozoic Amdo and Jiayuqiao microblocks in the Tibetan Plateau: Implications for Rodinia reconstruction. Geol. Soc. Am. Bull. 133, 663–678. https://doi.org/10.1130/B35632.1.
Yuan, S., Neubauer, F., Liu, Y., et al., 2020. Widespread Permian granite magmatism in Lower Austroalpine units: significance for Permian rifting in the Eastern Alps. Swiss. J. Geosci. 113, 18. https://doi.org/10.1186/s00015-020-00371-5.
Zhang, C.-L., Xian-Hua, L.i., Zheng-Xiang, L.i., Song-Nian, L.u., Hai-Min, Y.e., Hui-Min, L. i., 2007. Neoproterozoic ultramafic–mafic-carbonatite complex and granitoids in Quruqtagh of northeastern Tarim Block, western China: Geochronology, geochemistry and tectonic implications. Precambr. Res. https://doi.org/10.1016/J.PRECAMRES.2006.11.003.
Zhao, G., Cawood, P.A., Wilde, S.A., 2002. New constraints on the boundaries and age of the supercontinent Rodinia. Precambr. Res. 113 (3–4), 295–308.
Zhao, J.-H., Zhou, M.F., 2009. Secular evolution of the Neoproterozoic lithospheric mantle underneath the northern margin of the Yangtze Block, South China. Lithos 107 (3–4), 152–168.